IEEE Access
Multidisciplinary ⋮ Rapid Review ⋮ Open Access Journal

Received June 24, 2020, accepted July 7, 2020, date of publication July 28, 2020, date of current version August 10, 2020.

Digital Object Identifier 10.1109/ACCESS.2020.3012447

Radial Versus Cartesian Control Strategies to Stabilize the Nonlinear Whirling Motion of the Six-Pole Rotor-AMBs

NASSER A. SAEED[1], EMAD MAHROUS AWWAD[2,3], MOHAMMED A. EL-MELIGY[4], AND EMAD S. ABOUEL NASR[5,6]

[1]Department of Physics and Engineering Mathematics, Faculty of Electronic Engineering, Menoufia University, Menouf 32952, Egypt
[2]Department of Electrical Engineering, College of Engineering, King Saud University, Riyadh 11421, Saudi Arabia
[3]Department of Industrial Electronics and Control Engineering, Faculty of Electronic Engineering, Menoufia University, Menouf 32952, Egypt
[4]Advanced Manufacturing Institute, King Saud University, Riyadh 11421, Saudi Arabia
[5]Department of Industrial Engineering, College of Engineering, King Saud University, Riyadh 11421, Saudi Arabia
[6]Department of Mechanical Engineering, Faculty of Engineering, Helwan University, Cairo 11732, Egypt

Corresponding author: Emad Mahrous Awwad (emad.mahrous@el-eng.menofia.edu.eg)

This work was supported in part by the Researchers Supporting Project number (RSP-2020/164), King Saud University, Riyadh, Saudi Arabia.

ABSTRACT Rotor active magnetic bearings system is the most efficient supporting technique of high-speed rotating machinery. This work aims to explore the dynamical behaviors of the 6-pole rotor active magnetic bearings system for the first time. Two different control strategies are introduced to mitigate the considered system lateral vibrations and the corresponding whirling motions. The first control technique (Radial control) is suggested such that the attractive magnetic force in each pole is proportional to both the radial displacement and radial velocity of the rotating disk toward that pole. The second control strategy (Cartesian control) is proposed such that the controlled magnetic force in each pole is designed to be proportional to both the cartesian displacement and cartesian velocity of the rotating disk in two perpendicular directions. Based on the proposed control strategies, two nonlinear dynamical models are derived and then analyzed by applying perturbation methods. Different response-curves and bifurcation diagrams are plotted utilizing the disk spinning-speed and the disk eccentricity as bifurcation control parameters. The main obtained analytical and numerical results illustrated that the considered system can perform a circular forward whirling motion only under the first control technique, while four whirling modes (that are forward whirling, backward whirling, both forward and backward whirling, and oscillation along a straight line) are noticed in the second control method depending on the disk spinning speed. Moreover, it is found that the radial control method is robust against the system instability than the cartesian control one, especially at large disk eccentricity. However, the cartesian control method could exhibit a vibration suppression efficiency higher than the radial control one at small disk eccentricity.

INDEX TERMS Six-pole rotor-AMBs, radial control, Cartesian control, stability, whirling motion, response-curve, bifurcation diagram, frequency spectrum, Poincare map.

I. INTRODUCTION

Turbomachinery is a mechanical instrument that used to manage the mechanical-fluid energy transfer. Based on the energy transfer path, turbomachinery takes its name either a turbine or a compressor. The turbine is the mechanical instrument that converts the kinetic energy from fluids into rotational mechanical motion, while the compressor utilizes the mechanical energy to compress the fluids. Therefore, Turbomachinery is the generic name for any rotating machines. These machines have many industrial and engineering applications such as in aircraft, automotive, nuclear power plants, oil platforms…etc. According to the targeted engineering applications, turbomachinery may face less or more dangerous environmental conditions. For example, turbomachinery that employed for electric energy generation in nuclear power plants may suffer from earthquakes. Also, turbomachinery that used in the offshore oil production

The associate editor coordinating the review of this manuscript and approving it for publication was Haibin Sun.

This work is licensed under a Creative Commons Attribution 4.0 License. For more information, see https://creativecommons.org/licenses/by/4.0/

system, where huge sea waves can hit these boats resulting in large structural vibrations…etc. Therefore, turbomachinery should be designed to operate safely and to withstand all of these environmental circumstances. It is well known that the rotating shaft is the key part of the working principle of turbomachinery regardless of its type either turbines or compressors. The sustained rotation of this shaft is the major important engineering task that is carried out by bearings to provide a stator-rotor mechanical link. Three main types of bearings are provided that are fluid bearings, rolling element bearings, and Active Magnetic Bearings (AMBs). AMBs has many advantages over conventional bearings (i.e. fluid and rolling element bearings). The basic working principle of the AMBs is the magnetic suspension of the rotating shaft using controllable magnetic forces. Therefore, the AMBs system avoids any physical contact between the stator and the rotating shaft. Moreover, the energetic losses are limited, which ultimately improves the turbomachinery efficiency.

According to the electromagnetic theory, the attractive magnetic force is proportional to the square of the applied current in the coil and inversely proportional to the position of the rotor. Therefore, AMBs is an inherently nonlinear system, where every design for AMBs has its own dynamical behaviors. Therefore, many research articles have been dedicated to explore the nonlinear dynamics for different configurations of Rotor-AMBs [1]–[17]. Ji *et al.* [1] explored the nonlinear dynamical behaviors of the four-pole Rotor-AMBs. They utilized the normal-form method to investigate the derived mathematical model, where many nonlinear characteristics such as Hopf bifurcation, saddle-connection, and saddle-node are concluded. Many of the published articles investigated the nonlinear dynamical characteristics of the 8-pole Rotor-AMBs, where Ji *et al.* [2]–[4] studied the dynamical behaviors and the whirling motions of the 8-pole Rotor-AMBs. The authors applied the conventional PD-controller to stabilize the system vibrations. Based on the obtained analytical and numerical results, the authors reported many nonlinear phenomena such as jump phenomenon, bistable solution, and sensitivity to the initial conditions. Eissa *et al.* [5], and Saeed and Kandil [6] introduced more advanced control techniques to mitigate the lateral vibrations of the 8-pole Rotor-AMBs at primary resonance case. Eissa *et al.* [5] utilized the nonlinear saturation controller along with conventional PD-controller to suppress the system primary resonance vibrations at 1:2 internal resonance. Saeed and Kandil [6] applied the positive position feedback controller and the conventional PD-controller simultaneously to eliminate Rotor-AMBs primary resonance case at 1:1 internal resonance. Zhang *et al.* [7]–[9] introduced a modified version of the PD-controller to control the nonlinear behaviors of the 8-pole Rotor-AMBs. They assumed that the proportional gain coefficient (k_1) of the PD-controller has a periodic term such that $k_1 = k_0 + kcos(\omega t)$. On the other hand, many papers have been dedicated for lateral vibration analysis and control of the 16-pole Rotor-AMBs. Zhang *et al.* [10]–[12] explored the nonlinear dynamics of the 16-pole rotor AMBs with time varying stiffness. They applied the multiple time scales to obtain the amplitude-phase modulation equations at primary and subharmonic resonance cases. Based on the obtained results, the authors concluded that the system can exhibit period-2, period-3, period-11, quasi-periodic, and chaotic motions depending on the excitation force magnitude. Recently, Saeed *et al.* [13] introduced an analytical and numerical investigation for the nonlinear characteristics of constant stiffness coefficients 16-pole Rotor-AMBs. The author reported that the stiffness coefficients 16-pole Rotor-AMBs can exhibits one of quadri-stable motions depending on the initial conditions at the same spinning-speed. Tang *et al.* [14], [15] utilized the superconducting magnetic bearings and active magnetic bearing to stabilize the lateral oscillation of high–speed rotor system. They concluded that the cross-feedback control is one of the efficient control method in suppressing the considered system lateral vibrations. Du *et al.* [16] and Xu *et al.* [17] investigated the electromagnetic aspects of the rotor AMBs systems. Zheng *et al.* [18], [19], Yao *et al.* [20], and Gao *et al.* [21] introduced different advanced control techniques to stabilize the lateral vibrations of the rotor AMBs system.

Engineering applications of Rotor-AMBs are not limited to work as an excellent replacement for the conventional bearing only in high-speed rotating machinery. Several research articles have investigated many different applications for the Rotor- AMBs, where Ishida and Inoue [22] applied the 4-pole Rotor-AMBs as dynamic nonlinear vibration absorber to control the lateral oscillations of a vertically supported Jeffcott rotor system. In addition, Abdul-Hameed Saeed *et al.* [23]–[27] utilized the 4-pole Rotor-AMBs as an active actuator with different control algorithms to mitigate whirling motions of both the vertically and horizontally supported Jeffcott rotor systems. Srinivas *et al.* [28] summarized many engineering applications of Rotor-AMBs. Matsuda *et al.* [29] investigated relation between the electromagnetic poles number and the outside stator diameter for a constant load capacity of Rotor-AMBs. They found that the 6-pole Rotor-AMBs has small outside diameter than the 8-pole one for the same load capacity. Besides, it is found that the 3-pole Rotor-AMBs yield the smallest outside diameter.

Although the 6-pole Rotor-AMBs provides load capacity higher than the 8-pole one [29], the nonlinear vibratory characteristics of the 6-pole Rotor-AMBs have not investigated until now. Therefore, this article is intended to explore the nonlinear dynamics of the 6-pole Rotor-AMBs under two different control strategies. The first control technique (radial control) is proposed such that the controlled magnetic force in each pole is designed to be proportional to the radial displacement and velocity of the rotating disk toward that pole. The second control strategy (cartesian control) is designed such that the magnetic force in each pole is proportional to the cartesian displacement and velocity of the rotating disk in two perpendicular directions as shown in Fig.1.

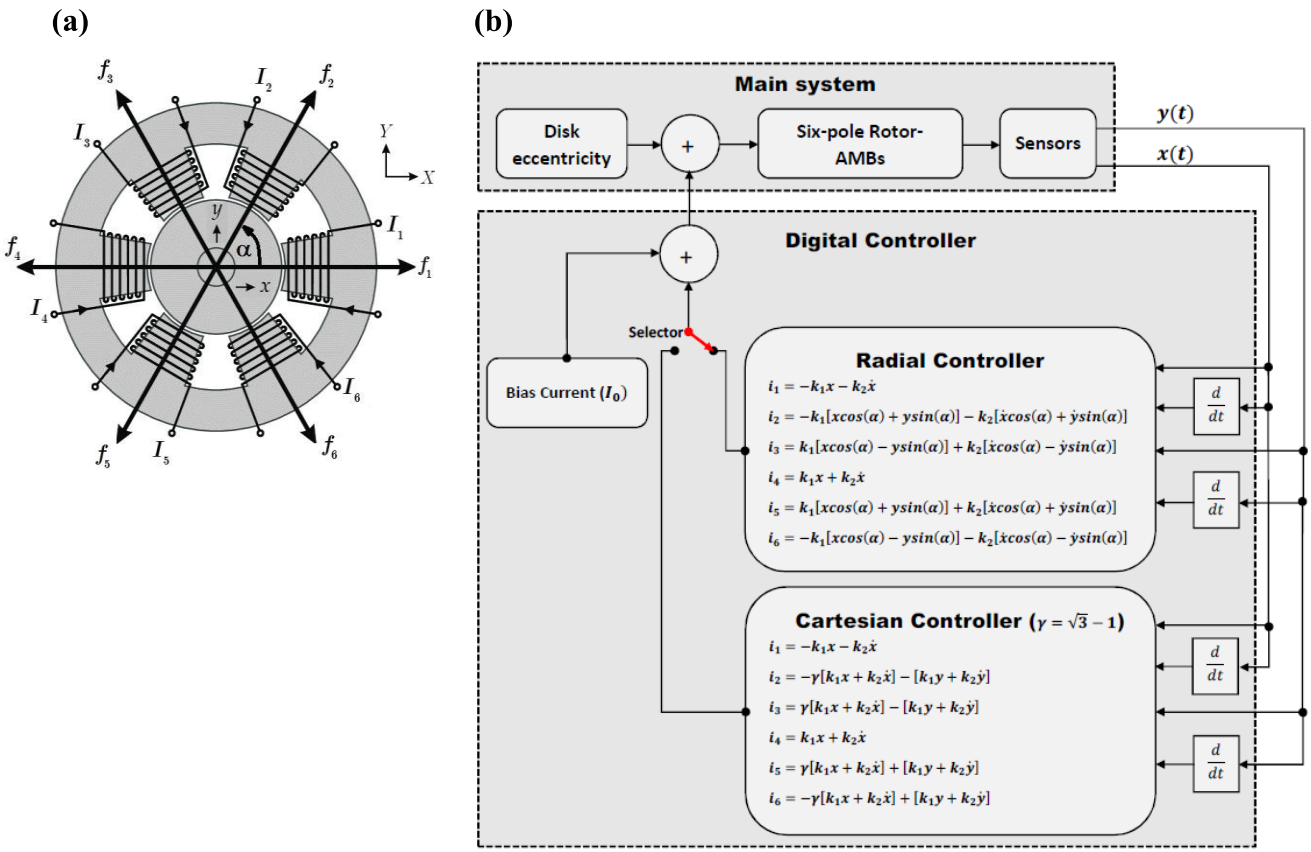

FIGURE 1. (a) 6-pole rotor active magnetic bearing system, (b) Schematic diagram showing the applied control methods.

The complete system model for each control method is derived in its normalized form and then analyzed. The effect of the different control parameters on the system lateral vibrations is explored. The obtained analytical and numerical results illustrated that the considered system can perform a circular forward whirling motion only under the first control technique, while four whirling modes (that are forward whirling, backward whirling, both forward and backward whirling, and oscillation along a straight line) are noticed in the second control method depending on the disk spinning speed. Moreover, it is found that the radial control method is robust against the system instability than the cartesian control one, especially at large disk eccentricity. However, the cartesian control method could exhibit a vibration suppression efficiency higher than the radial control one at small disk eccentricity. Accordingly, the online switching process from one of the control methods to the other is numerically validated. The numerical simulations confirmed the possibility of the smooth transition from the radial control method to the cartesian one and vice versa. Therefore, it is recommended to implement the two control strategies on a digital controller that can be programmed to switch between them depending on the required operational conditions.

II. EQUATIONS OF MOTION

The 6-pole Rotor-AMBs is considered as a rigid body lamped parameter system that is supported via six controllable magnetic forces ($f_i, i = 1, 2, \ldots, 6$) as shown in Fig.1a. Accordingly, the mathematical model governing the system oscillations in X- and Y directions can be expressed as follows [30], [31]:

$$m\ddot{x} + \mu\dot{x} - F_x = mE\vartheta^2\cos(\vartheta\tau), \tag{1.1}$$
$$m\ddot{y} + \mu\dot{y} - F_y = mE\vartheta^2\sin(\vartheta\tau). \tag{1.2}$$

where m is the mass of the rotating disk, E is the eccentricity of the rotor, μ is the linear damping coefficient in $X-$ and $Y-$directions, ϑ is the angular speed of the rotating disk, $F_x = f_1 - f_4 + (f_2 + f_6 - f_3 - f_5)\cos(\alpha)$ and $F_y = (f_2 + f_3 - f_5 - f_6)\sin(\alpha)$ are the net electromagnetic magnetic forces in $X-$ and $Y-$ directions, and $\alpha = \frac{\pi}{3}$ is the angle between every two consecutive poles. It is assumed that the 6-pole Rotor-AMBs is a symmetric system. According to the electromagnetic theory, the mathematical model that governs the electromagnetic force in each pole is given as [31]:

$$f_j = \frac{1}{4}\mu_0 N^2 A\cos(\varphi)\frac{I_j^2}{h_j^2}, \quad j = 1, 2, \ldots, 6 \tag{2}$$

where A is the effective cross-sectional area of one electromagnet pole, N is the electromagnetic pole windings number, μ_0 is the air electromagnetic permeability, φ is the corresponding half-angle of the radial electromagnetic circuit, I_j is the electric current that flows thought the jth pole, and h_j are the dynamic air-gap between the rotating disk and the jth pole. The dynamic air-gab h_j ($j = 1, 2, \ldots, 6$) for small disk displacements x and y away from the origin can be expressed as:

$$\left.\begin{array}{ll} h_j = s_0 \mp x, & j = 1, 4 \\ h_j = s_0 \mp x\cos(\alpha) \mp y\sin(\alpha), & j = 2, 5 \\ h_j = s_0 \pm x\cos(\alpha) \mp y\sin(\alpha), & j = 3, 6 \end{array}\right\} \tag{3}$$

where s_0 is the static air-gap between the poles and the rotating disk when the disk displacements x and y are zeros. The electric current in each pole is defined as follows:

$$I_j = I_0 + i_j, \quad j = 1, 2, \ldots, 6 \tag{4}$$

where I_0 is the bias current, and i_j is the control current in j^{th} pole.

A. RADIAL CONTROL STRATEGY MATHEMATICAL MODEL

In the radial control strategy, the control algorithm is suggested such that the control current i_j in each pole is designed to be proportional to both the radial displacement and radial velocity of the rotating disk as follows:

$$\left.\begin{array}{ll} i_j = \mp k_1 x \mp k_2 \dot{x}, & j = 1, 4 \\ i_j = \mp k_1 \left(x\cos(\alpha) + y\sin(\alpha)\right) & \\ \quad \mp k_2 \left(\dot{x}\cos(\alpha) + \dot{y}\sin(\alpha)\right), & j = 2, 5 \\ i_j = \pm k_1 \left(x\cos(\alpha) - y\sin(\alpha)\right) & \\ \quad \pm k_2 \left(\dot{x}\cos(\alpha) - \dot{y}\sin(\alpha)\right), & j = 3, 6 \end{array}\right\} \tag{5}$$

where, k_1 is the proportional control gain and k_2 is the derivative control gain. Substituting Eqs. (3), (4) and (5) into Eq. (2), we get

$$f_1 = \frac{1}{4}\mu_0 N^2 A\cos(\varphi)\left(\frac{I_0 - k_1 x - k_2\dot{x}}{s_0 - x}\right)^2, \tag{6.1}$$

$$f_2 = \frac{1}{4}\mu_0 N^2 A\cos(\varphi)\left(\frac{I_0 - k_1\left(x\cos(\alpha) + y\sin(\alpha)\right)}{s_0 - x\cos(\alpha) - y\sin(\alpha)} - \frac{k_2\left(\dot{x}\cos(\alpha) + \dot{y}\sin(\alpha)\right)}{s_0 - x\cos(\alpha) - y\sin(\alpha)}\right)^2, \tag{6.2}$$

$$f_3 = \frac{1}{4}\mu_0 N^2 A\cos(\varphi)\left(\frac{I_0 + k_1\left(x\cos(\alpha) - y\sin(\alpha)\right)}{s_0 + x\cos(\alpha) - y\sin(\alpha)} + \frac{k_2\left(\dot{x}\cos(\alpha) - \dot{y}\sin(\alpha)\right)}{s_0 + x\cos(\alpha) - y\sin(\alpha)}\right)^2, \tag{6.3}$$

$$f_4 = \frac{1}{4}\mu_0 N^2 A\cos(\varphi)\left(\frac{I_0 + k_1 x + k_2\dot{x}}{s_0 + x}\right)^2, \tag{6.4}$$

$$f_5 = \frac{1}{4}\mu_0 N^2 A\cos(\varphi)\left(\frac{I_0 + k_1\left(x\cos(\alpha) + y\sin(\alpha)\right)}{s_0 + x\cos(\alpha) + y\sin(\alpha)} + \frac{k_2\left(\dot{x}\cos(\alpha) + \dot{y}\sin(\alpha)\right)}{s_0 + x\cos(\alpha) + y\sin(\alpha)}\right)^2, \tag{6.5}$$

$$f_6 = \frac{1}{4}\mu_0 N^2 A\cos(\varphi)\left(\frac{I_0 - k_1\left(x\cos(\alpha) - y\sin(\alpha)\right)}{s_0 - x\cos(\alpha) + y\sin(\alpha)} - \frac{k_2\left(\dot{x}\cos(\alpha) - \dot{y}\sin(\alpha)\right)}{s_0 - x\cos(\alpha) + y\sin(\alpha)}\right)^2. \tag{6.6}$$

According to the schematic diagram of the 6-pole Rotor-AMBs given in Fig. 1a, the net electromagnetic forces in X and Y directions after expanding denominators of Eqs (6) using Mclaurin series up to the third-order approximation, can be expressed as follows [1]–[13]:

$$\begin{aligned} F_x &= f_1 - f_4 + (f_2 + f_6 - f_3 - f_5)\cos(\alpha) \\ &= \frac{1}{4}\mu_0 N^2 A\cos(\varphi)\Bigg[\frac{8k_2^2\cos^2(\alpha)\sin^2(\alpha)x\dot{y}^2}{s_0^3} \\ &\quad + \frac{16k_1k_2\cos^4(\alpha)x^2\dot{x}}{s_0^3} + \frac{24k_1^2\cos^2(\alpha)\sin^2(\alpha)xy^2}{s_0^3} \\ &\quad - \frac{8I_0k_2\cos^2(\alpha)\dot{x}}{s_0^2} - \frac{8I_0k_1\cos^2(\alpha)x}{s_0^2} \\ &\quad + \frac{8k_1^2\cos^4(\alpha)x^3}{s_0^3} + \frac{16I_0^2\cos^4(\alpha)x^3}{s_0^5} + \frac{8I_0^2x^3}{s_0^5} \\ &\quad + \frac{4I_0^2x}{s_0^3} + \frac{4k_1^2x^3}{s_0^3} - \frac{24I_0k_2\cos^4(\alpha)x^2\dot{x}}{s_0^4} \\ &\quad - \frac{24I_0k_1\cos^4(\alpha)x^3}{s_0^4} - \frac{48I_0k_2\cos^2(\alpha)\sin^2(\alpha)xy\dot{y}}{s_0^4} \\ &\quad + \frac{8k_2^2\cos^4(\alpha)x\dot{x}^2}{s_0^3} + \frac{16k_1k_2\cos^2(\alpha)\sin^2(\alpha)\dot{x}y^2}{s_0^3} \\ &\quad + \frac{16k_2^2\cos^2(\alpha)\sin^2(\alpha)\dot{x}y\dot{y}}{s_0^3} + \frac{8I_0^2\cos^2(\alpha)x}{s_0^3} \\ &\quad - \frac{72I_0k_1\cos^2(\alpha)\sin^2(\alpha)xy^2}{s_0^4} + \frac{4k_2^2x\dot{x}^2}{s_0^3} \\ &\quad - \frac{24I_0k_2\cos^2(\alpha)\sin^2(\alpha)\dot{x}y^2}{s_0^4} - \frac{4I_0k_1x}{s_0^2} \\ &\quad + \frac{48I_0^2\cos^2(\alpha)\sin^2(\alpha)xy^2}{s_0^5} - \frac{4I_0k_2\dot{x}}{s_0^2} \\ &\quad + \frac{32k_1k_2\cos^2(\alpha)\sin^2(\alpha)xy\dot{y}}{s_0^3} - \frac{12I_0k_1x^3}{s_0^4} \\ &\quad - \frac{12I_0k_2x^2\dot{x}}{s_0^4} + \frac{8k_1k_2x^2\dot{x}}{s_0^3}\Bigg], \end{aligned} \tag{7.1}$$

$$\begin{aligned} F_y &= (f_2 + f_3 - f_5 - f_6)\sin(\alpha) \\ &= \frac{1}{4}\mu_0 N^2 A\cos(\varphi)\Bigg[\frac{24k_1^2\cos^2(\alpha)\sin^2(\alpha)x^2y}{s_0^3} \\ &\quad + \frac{8k_1^2\sin^4(\alpha)y^3}{s_0^3} + \frac{16k_1k_2\sin^4(\alpha)y^2\dot{y}}{s_0^3} \\ &\quad + \frac{16k_1k_2\cos^2(\alpha)\sin^2(\alpha)x^2\dot{y}}{s_0^3} - \frac{8I_0k_1\sin^2(\alpha)y}{s_0^2} \\ &\quad + \frac{32k_1k_2\cos^2(\alpha)\sin^2(\alpha)x\dot{x}y}{s_0^3} - \frac{8I_0k_2\sin^2(\alpha)\dot{y}}{s_0^2} \end{aligned}$$

$$+\frac{16k_2^2\cos^2(\alpha)\sin^2(\alpha)x\dot{x}\dot{y}}{s_0^3}-\frac{24I_0k_1\sin^4(\alpha)y^3}{s_0^4}$$
$$-\frac{72I_0k_1\cos^2(\alpha)\sin^2(\alpha)x^2\dot{y}}{s_0^4}+\frac{8I_0^2\sin^2(\alpha)y}{s_0^3}$$
$$-\frac{24I_0k_2\cos^2(\alpha)\sin^2(\alpha)x^2\dot{y}}{s_0^4}+\frac{8k_2^2\sin^4(\alpha)y\dot{y}^2}{s_0^3}$$
$$+\frac{8k_2^2\cos^2(\alpha)\sin^2(\alpha)\dot{x}^2y}{s_0^3}-\frac{24I_0k_2\sin^4(\alpha)y^2\dot{y}}{s_0^4}$$
$$-\frac{48I_0k_2\cos^2(\alpha)\sin^2(\alpha)x\dot{x}y}{s_0^4}+\frac{16I_0^2\sin^4(\alpha)y^3}{s_0^5}$$
$$+\frac{48I_0^2\cos^2(\alpha)\sin^2(\alpha)x^2y}{s_0^5}\Bigg]. \tag{7.2}$$

Substituting Eqs. (7) into equations (1), with introducing the new dimensionless parameters $t=\omega_n\tau$, $u=\frac{x}{s_0}$, $v=\frac{y}{s_0}$, $\dot{u}=\frac{\dot{x}}{\omega_n s_0}$, $\dot{v}=\frac{\dot{y}}{\omega_n s_0}$, $\ddot{u}=\frac{\ddot{x}}{\omega_n^2 s_0}$, $\ddot{v}=\frac{\ddot{y}}{\omega_n^2 s_0}$, $\omega_n=\sqrt{\frac{\mu_0 I_0^2 N^2 A\cos(\varphi)}{4ms_0^3}}$, $c_1=\frac{\mu}{\omega_n m}$, $p=\frac{s_0}{I_0}k_1$, $d=\frac{s_0\omega_n}{I_0}k_2$, $f=\frac{E}{s_0}$, and $\Omega=\frac{\vartheta}{\omega_n}$, it is possible to rearrange Eqs (1) in their new dimensionless form as:

$$\ddot{u}+\mu_1\dot{u}+\omega_1^2u-\Big(\beta_{11}u^3+\beta_{12}u^2\dot{u}+\beta_{13}u\dot{u}^2+\beta_{14}uv^2+\beta_{15}uv\dot{v}+\beta_{16}u\dot{v}^2+\beta_{17}\dot{u}v^2+\beta_{18}\dot{u}v\dot{v}\Big)=f\Omega^2\cos(\Omega t), \tag{8.1}$$

$$\ddot{v}+\mu_2\dot{v}+\omega_2^2v-\Big(\beta_{21}v^3+\beta_{22}v^2\dot{v}+\beta_{23}v\dot{v}^2+\beta_{24}vu^2+\beta_{25}vu\dot{u}+\beta_{26}v\dot{u}^2+\beta_{27}\dot{v}u^2+\beta_{28}\dot{v}u\dot{u}\Big)=f\Omega^2\sin(\Omega t). \tag{8.2}$$

where, $\mu_1=\mu_2=\mu+6d$, $\omega_1=\omega_2=\sqrt{6(p-1)}$, $\beta_{11}=\beta_{21}=9-\frac{27}{2}p+\frac{9}{2}p^2$, $\beta_{12}=\beta_{22}=9pd-\frac{27}{2}d$, $\beta_{13}=\beta_{23}=\frac{9}{2}d^2$, $\beta_{14}=\beta_{24}=\frac{9}{2}\left(2-3p+p^2\right)$, $\beta_{15}=\beta_{25}=6pd-9d$, $\beta_{16}=\beta_{26}=\frac{3}{2}d^2$, $\beta_{17}=\beta_{27}=3pd-\frac{9}{2}d$, $\beta_{18}=\beta_{28}=3d^2$.

B. CARTESIAN CONTROL STRATEGY MATHEMATICAL MODEL

The system is designed such that the 6-poles interact together to control Rotor-AMBs lateral vibrations in $X-$direction, while the only nonhorizontal poles (i.e. f_2, f_3, f_5, and f_6) are responsible for the system oscillations in $Y-$direction. In this control strategy, the control algorithm is proposed such that the control current i_j in each pole is designed to be proportional to both the cartesian displacement and cartesian velocity of the rotating disk in X and $Y-$directions. Accordingly, the control current in each pole can be expressed as follows:

$$\left.\begin{aligned} i_j &= \mp k_1x\mp k_2\dot{x}, & j=1,4\\ i_j &= \mp\gamma(k_1x+k_2\dot{x})\mp(k_1y+k_2\dot{y}), & j=2,5\\ i_j &= \pm\gamma(k_1x+k_2\dot{x})\mp(k_1y+k_2\dot{y}). & j=3,6\end{aligned}\right\} \tag{9}$$

where γ is a dimensionless parameter that determines the ratio of the control current in $X-$direction that can flow through the non-horizontal poles (i.e. f_2, f_3, f_5, and f_6). Substituting Eqs. (3), (4) and (9) into Eq. (2), we get

$$f_1=\frac{1}{4}\mu_0N^2A\cos(\varphi)\left(\frac{I_0-k_1x-k_2\dot{x}}{s_0-x}\right)^2, \tag{10.1}$$

$$f_2=\frac{1}{4}\mu_0N^2A\cos(\varphi)\left(\frac{I_0-\gamma k_1x-\gamma k_2\dot{x}-k_1y-k_2\dot{y}}{s_0-x\cos(\alpha)-y\sin(\alpha)}\right)^2, \tag{10.2}$$

$$f_3=\frac{1}{4}\mu_0N^2A\cos(\varphi)\left(\frac{I_0+\gamma k_1x+\gamma k_2\dot{x}-k_1y-k_2\dot{y}}{s_0+x\cos(\alpha)-y\sin(\alpha)}\right)^2, \tag{10.3}$$

$$f_4=\frac{1}{4}\mu_0N^2A\cos(\varphi)\left(\frac{I_0+k_1x+k_2\dot{x}}{s_0+x}\right)^2, \tag{10.4}$$

$$f_5=\frac{1}{4}\mu_0N^2A\cos(\varphi)\left(\frac{I_0+\gamma k_1x+\gamma k_2\dot{x}+k_1y+k_2\dot{y}}{s_0+x\cos(\alpha)+y\sin(\alpha)}\right)^2, \tag{10.5}$$

$$f_6=\frac{1}{4}\mu_0N^2A\cos(\varphi)\left(\frac{I_0-\gamma k_1x-\gamma k_2\dot{x}+k_1y+k_2\dot{y}}{s_0-x\cos(\alpha)+y\sin(\alpha)}\right)^2. \tag{10.6}$$

Accordingly, the total electromagnetic forces in X and $Y-$directions after expanding denominators of Eqs (10) using Mclaurin series up to the third-order approximation, can be expressed as follows [1]–[13]:

$$\begin{aligned}F_x=\frac{1}{4}\mu_0N^2A\cos(\varphi)\Bigg[&+\frac{16\gamma k_1k_2\sin(\alpha)\cos(\alpha)\dot{x}y^2}{s_0^3}\\
&-\frac{24\gamma I_0k_2\sin^2(\alpha)\cos(\alpha)\dot{x}y^2}{s_0^4}+\frac{4k_2^2x\dot{x}^2}{s_0^3}\\
&-\frac{24\gamma I_0k_1\sin^2(\alpha)\cos(\alpha)xy^2}{s_0^4}-\frac{4I_0k_2\dot{x}}{s_0^2}\\
&+\frac{16\gamma k_1^2\sin(\alpha)\cos(\alpha)xy^2}{s_0^3}+\frac{8k_1k_2x^2\dot{x}}{s_0^3}\\
&-\frac{48I_0k_2\sin(\alpha)\cos^2(\alpha)xy\dot{y}}{s_0^4}-\frac{12I_0k_2x^2\dot{x}}{s_0^4}\\
&+\frac{8\gamma^2k_1^2\cos(\alpha)x^3}{s_0^3}+\frac{8k_1^2\cos^2(\alpha)xy^2}{s_0^3}\\
&+\frac{8k_2^2\cos^2(\alpha)x\dot{y}^2}{s_0^3}+\frac{4k_1^2x^3}{s_0^3}+\frac{4I_0^2x}{s_0^3}+\frac{8I_0^2x^3}{s_0^5}\\
&+\frac{16\gamma k_1k_2\sin(\alpha)\cos(\alpha)xy\dot{y}}{s_0^3}-\frac{12I_0k_1x^3}{s_0^4}\\
&+\frac{16\gamma k_2^2\sin(\alpha)\cos(\alpha)\dot{x}y\dot{y}}{s_0^3}-\frac{4I_0k_1x}{s_0^2}\\
&+\frac{16k_1k_2\cos^2(\alpha)xy\dot{y}}{s_0^3}+\frac{8\gamma^2k_2^2\cos^2(\alpha)x\dot{x}^2}{s_0^3}\\
&-\frac{24\gamma I_0k_2\cos^3(\alpha)x^2\dot{x}}{s_0^4}+\frac{16I_0^2\cos^4(\alpha)x^3}{s_0^5}\\
&-\frac{48I_0k_1\sin(\alpha)\cos^2(\alpha)xy^2}{s_0^4}+\frac{8I_0^2\cos^2(\alpha)x}{s_0^3}\end{aligned}$$

$$+\frac{16\gamma^2 k_1 k_2 \cos^2(\alpha)x^2\dot{x}}{s_0^3} - \frac{8\gamma I_0 k_1 \cos(\alpha)x}{s_0^2} - \frac{8\gamma I_0 k_2 \cos(\alpha)\dot{x}}{s_0^2} - \frac{24\gamma I_0 k_1 \cos^3(\alpha)x^3}{s_0^4} + \frac{48 I_0^2 \sin^2(\alpha)\cos^2(\alpha)xy^2}{s_0^5}\Bigg], \tag{11.1}$$

$$F_y = \frac{1}{4}\mu_0 N^2 A\cos(\varphi)\Bigg[\frac{16\gamma k_1 k_2 \sin(\alpha)\cos(\alpha)\dot{y}x^2}{s_0^3} + \frac{16\gamma k_1^2 \sin(\alpha)\cos(\alpha)yx^2}{s_0^3} + \frac{8\gamma^2 k_1^2 \sin^2(\alpha)yx^2}{s_0^3} + \frac{16\gamma^2 k_1 k_2 \sin^2(\alpha)yx\dot{x}}{s_0^3} - \frac{24 I_0 k_2 \sin^3(\alpha)y^2\dot{y}}{s_0^4} - \frac{48\gamma I_0 k_1 \sin^2(\alpha)\cos(\alpha)yx^2}{s_0^4} + \frac{8k_1^2 \sin^2(\alpha)y^3}{s_0^3} + \frac{16 k_1 k_2 \sin^2(\alpha)y^2\dot{y}}{s_0^3} + \frac{8\gamma^2 k_2^2 \sin^2(\alpha)y\dot{x}^2}{s_0^3} + \frac{48 I_0^2 \sin^2(\alpha)\cos^2(\alpha)yx^2}{s_0^5} + \frac{16 I_0^2 \sin^4(\alpha)y^3}{s_0^5} - \frac{48\gamma I_0 k_2 \sin^2(\alpha)\cos(\alpha)yx\dot{x}}{s_0^4} + \frac{8 I_0^2 \sin^2(\alpha)y}{s_0^3} + \frac{16\gamma k_1 k_2 \sin(\alpha)\cos(\alpha)yx\dot{x}}{s_0^3} - \frac{8 I_0 k_1 \sin(\alpha)y}{s_0^2} + \frac{16\gamma k_2^2 \sin(\alpha)\cos(\alpha)\dot{y}x\dot{x}}{s_0^3} - \frac{8 I_0 k_2 \sin(\alpha)\dot{y}}{s_0^2} - \frac{24 I_0 k_1 \sin(\alpha)\cos^2(\alpha)x^2 y}{s_0^4} + \frac{8k_2^2 \sin^2(\alpha)y\dot{y}^2}{s_0^3} - \frac{24 I_0 k_2 \sin(\alpha)\cos^2(\alpha)x^2\dot{y}}{s_0^4} - \frac{24 I_0 k_1 \sin^3(\alpha)y^3}{s_0^4}\Bigg]. \tag{11.2}$$

Substituting Eqs. (11) into Eqs. (1), with introducing dimensionless parameters $t = \omega_n\tau$, $u = \frac{x}{s_0}$, $v = \frac{y}{s_0}$, $\dot{u} = \frac{\dot{x}}{\omega_n s_0}$, $\dot{v} = \frac{\dot{y}}{\omega_n s_0}$, $\ddot{u} = \frac{\ddot{x}}{\omega_n^2 s_0}$, $\ddot{v} = \frac{\ddot{y}}{\omega_n^2 s_0}$, $\omega_n = \sqrt{\frac{\mu_0 I_0^2 N^2 A\cos(\varphi)}{4ms_0^3}}$, $c_1 = \frac{\mu}{\omega_n m}$, $p = \frac{s_0}{I_0}k_1$, $d = \frac{s_0\omega_n}{I_0}k_2$, $f = \frac{E}{s_0}$, and $\Omega = \frac{\vartheta}{\omega_n}$, we get

$$\ddot{u} + \mu_1\dot{u} + \omega_1^2 u - \Big(\beta_{11}u^3 + \beta_{12}u^2\dot{u} + \beta_{13}u\dot{u}^2 + \beta_{14}uv^2 + \beta_{15}uv\dot{v} + \beta_{16}u\dot{v}^2 + \beta_{17}\dot{u}v^2 + \beta_{18}\dot{u}v\dot{v}\Big) = f\Omega^2\cos(\Omega t), \tag{12.1}$$

$$\ddot{v} + \mu_2\dot{v} + \omega_2^2 v - \Big(\beta_{21}v^3 + \beta_{22}v^2\dot{v} + \beta_{23}v\dot{v}^2 + \beta_{24}vu^2 + \beta_{25}vu\dot{u} + \beta_{26}v\dot{u}^2 + \beta_{27}\dot{v}u^2 + \beta_{28}\dot{v}u\dot{u}\Big) = f\Omega^2\sin(\Omega t). \tag{12.2}$$

where $\mu_1 = \mu + 4d(\gamma+1)$, $\mu_2 = \mu + 4\sqrt{3}\,d$, $\omega_1 = \sqrt{4p(\gamma+1)-6}$, $\omega_2 = \sqrt{4\sqrt{3}\,p-6}$, $\beta_{11} = 9 - 3p(\gamma+4) + 4p^2(\gamma^2+1)$, $\beta_{21} = 9 + 6p^2 - 3^{\frac{5}{2}}p$, $\beta_{12} = 4pd(2+\gamma^2) - 6d(2+\gamma)$, $\beta_{22} = 12pd - 3^{\frac{5}{2}}d$, $\beta_{13} = 2d^2(2+\gamma^2)$, $\beta_{23} = 16d^2$, $\beta_{14} = \left(4\sqrt{3}\gamma+2\right)p^2 - \left(9\gamma+6\sqrt{3}\right)p + 9$, $\beta_{24} = \left(6\gamma+4\sqrt{3}\right)\gamma p^2 - \left(18\gamma+3\sqrt{3}\right)p + 9$, $\beta_{15} = 4\left(\sqrt{3}\gamma+1\right)pd - 6\sqrt{3}\,d$, $\beta_{25} = 4\left(3\gamma+\sqrt{3}\right)\gamma pd - 18\gamma d$, $\beta_{16} = 2d^2$, $\beta_{26} = 6\gamma^2 d^2$, $\beta_{17} = \left(4\sqrt{3}\,p-9\right)\gamma d$, $\beta_{27} = \left(4\sqrt{3}\gamma p - 3\sqrt{3}\right)d$, and $\beta_{18} = \beta_{28} = 4\sqrt{3}\gamma d^2$.

The obtained mathematical models that govern the system motion in both the radial and cartesian control methods (i.e. Eqs (8) and Eqs (12)) clearly have the same mathematical form but with different parameters definitions. It is worth to mention that the authors do this formulation intentionally to analyze the two models as a single one.

III. NONLINEAR ANALYSIS

The obtained mathematical models that govern dynamical behaviors of the 6-pole Rotor-AMBs in both the radial and cartesian control strategies have the same mathematical form. Therefore, Eqs (8) only have been analyzed as a general case. As the obtained mathematical models (i.e. Eqs (8) and Eqs (12)) are nonlinear ordinary differential equations that have not closed-form solution, there are different solution techniques for analyzing such systems [32]–[36]. However, the multiple time scales perturbation method is applied in this article to obtain the averaged equations that govern the oscillation amplitudes and the corresponding phase angles of the considered system. Accordingly, the solutions of Eqs. (8) can be sought as follows [36]:

$$u(t,\varepsilon) = u_1(T_0,T_1) + \varepsilon u_2(T_0,T_1) + O(\varepsilon^2), \tag{13.1}$$
$$v(t,\varepsilon) = v_1(T_0,T_1) + \varepsilon v_2(T_0,T_1) + O(\varepsilon^2). \tag{13.2}$$

where $\varepsilon \ll 1$ is a small book-keeping perturbation parameter, and $T_0 = t$, $T_1 = \varepsilon t$ are two time-scales that describe the system fast and slow dynamics. In terms of T_0 and T_1, the ordinary derivatives can be expressed in terms of the partial derivatives as:

$$\frac{d}{dt} = D_0 + \varepsilon D_1, \quad \frac{d^2}{dt^2} = D_0^2 + 2\varepsilon D_0 D_1, \quad D_j = \frac{\partial}{\partial T_j}, \quad j = 0, 1 \tag{14}$$

As Eqs (8) comprise odd nonlinearities only, the system parameters should be scaled as follows:

$$f = \varepsilon\hat{f}, \quad \mu_1 = \varepsilon\hat{\mu}_1, \ \mu_2 = \varepsilon\hat{\mu}_2, \ \beta_{ij} = \varepsilon\hat{\beta}_{ij}; \quad i = 1, 2, \quad j = 1, 2, \ldots, 8. \tag{15}$$

Substituting Eqs (13) to (15) into Eqs. (8) and comparing the coefficients that have the powers of ε, we get:
$O(\varepsilon^0)$:

$$(D_0^2 + \omega_1^2)u_1 = 0, \tag{16.1}$$
$$(D_0^2 + \omega_2^2)v_1 = 0. \tag{16.2}$$

$O(\varepsilon^1)$:

$$\begin{aligned}(D_0^2+\omega_1^2)u_2 = &-2D_0D_1u_1-\hat{\mu}_1D_0u_1+\hat{\beta}_{11}u_1^3\\ &+\hat{\beta}_{12}u_1^2(D_0u_1)+\hat{\beta}_{13}u_1(D_0u_1)^2\\ &+\hat{\beta}_{14}u_1v_1^2+\hat{\beta}_{15}u_1v_1(D_0v_1)\\ &+\hat{\beta}_{16}u_1(D_0v_1)^2+\hat{\beta}_{17}(D_0u_1)v_1^2\\ &+\hat{\beta}_{18}(D_0u_1)v_1(D_0v_1)+\hat{f}\Omega^2\cos(\Omega T_0),\end{aligned} \tag{17.1}$$

$$\begin{aligned}(D_0^2+\omega_2^2)v_2 = &-2D_0D_1v_1-\hat{\mu}_2D_0v_1+\hat{\beta}_{21}v_1^3\\ &+\hat{\beta}_{22}v_1^2(D_0v_1)+\hat{\beta}_{23}v_1(D_0v_1)^2\\ &+\hat{\beta}_{24}v_1u_1^2+\hat{\beta}_{25}v_1u_1(D_0u_1)\\ &+\hat{\beta}_{26}v_1(D_0u_1)^2+\hat{\beta}_{27}(D_0v_1)u_1^2\\ &+\hat{\beta}_{28}(D_0v_1)u_1(D_0u_1)+\hat{f}\Omega^2\sin(\Omega T_0).\end{aligned} \tag{17.2}$$

The solutions of Eqs. (16) can be expressed as:

$$u_1(T_0,T_1) = F_1(T_1)e^{i\omega_1T_0}+\overline{F_1}(T_1)e^{-i\omega_1T_0}, \tag{18.1}$$
$$v_1(T_0,T_1) = F_2(T_1)e^{i\omega_2T_0}+\overline{F_2}(T_1)e^{-i\omega_2T_0}. \tag{18.2}$$

where $F_1(T_1)$ and $F_2(T_1)$ are two unknown functions of the slow time scale T_1. Inserting Eqs (18) into Eqs (17) and following the same procedure (see [4]–[6]), we concluded that the considered system may be exhibit the resonance cases **a.** Primary resonance (when $\Omega \cong \omega_1$ or $\Omega \cong \omega_2$) **b.** Internal resonance (when $\omega_1 \cong \omega_2$) **c.** Simultaneous resonance (when $\Omega \cong \omega_1 \cong \omega_2$). To explore the vibrational behaviors of the considered system in the simultaneous resonance case, two new parameters σ_1 and σ_2 that known as detuning parameters to quantify the closeness between and the disk spinning-speed (Ω) and the natural frequencies (ω_1 and ω_2) of the 6-pole Rotor-AMBs are introduced as follows:

$$\Omega = \omega_1+\sigma_1 = \omega_1+\varepsilon\hat{\sigma}_1, \quad \omega_2 = \omega_1+\sigma_2 = \omega_1+\varepsilon\hat{\sigma}_2. \tag{19}$$

Substituting Eqs (18) and (19) into Eqs (17) with following the same procedure (see [4]–[6]), assuming that $F_1(T_1) = \frac{1}{2}a_1e^{i\phi_1}$ and $F_2(T_1) = \frac{1}{2}a_2e^{i\phi_2}$, we can derive the following averaged equations:

$$\begin{aligned}\frac{d}{dt}a_1 = &-\frac{1}{2}\mu_1a_1+\frac{1}{8}\beta_{12}a_1^3+\frac{1}{8\omega_1}\beta_{14}a_1a_2^2\sin(2\delta_1\\ &-2\delta_2)+\frac{1}{8\omega_1}\beta_{15}\omega_2a_1a_2^2\cos(2\delta_1-2\delta_2)\\ &-\frac{1}{8\omega_1}\beta_{16}\omega_2^2a_1a_2^2\sin(2\delta_1-2\delta_2)+\frac{1}{4}\beta_{17}a_1a_2^2\\ &-\frac{1}{8}\beta_{17}a_1a_2^2\cos(2\delta_1-2\delta_2)+\frac{1}{8}\beta_{18}\omega_2a_1a_2^2\\ &\times\sin(2\delta_1-2\delta_2)+\frac{1}{2\omega_1}f\Omega^2\sin(\delta_1),\end{aligned} \tag{20.1}$$

$$\begin{aligned}\frac{d}{dt}a_2 = &-\frac{1}{2}\mu_2a_2+\frac{1}{8}\beta_{22}a_2^3+\frac{1}{8\omega_2}\beta_{24}a_2a_1^2\sin(2\delta_2\\ &-2\delta_1)+\frac{1}{8\omega_2}\beta_{25}\omega_1a_2a_1^2\cos(2\delta_2-2\delta_1)\\ &-\frac{1}{8\omega_2}\beta_{26}\omega_1^2a_2a_1^2\sin(2\delta_2-2\delta_1)+\frac{1}{4}\beta_{27}a_2a_1^2\\ &-\frac{1}{8}\beta_{27}a_2a_1^2\cos(2\delta_2-2\delta_1)+\frac{1}{8}\beta_{28}\omega_1a_2a_1^2\\ &\times\sin(2\delta_2-2\delta_1)-\frac{1}{2\omega_2}f\Omega^2\cos(\delta_2),\end{aligned} \tag{20.2}$$

$$\begin{aligned}\frac{d}{dt}\delta_1 = &\sigma_1+\frac{3}{8\omega_1}\beta_{11}a_1^2+\frac{1}{8}\beta_{13}\omega_1a_1^2+\frac{1}{4\omega_1}\beta_{14}a_2^2\\ &+\frac{1}{8\omega_1}\beta_{14}a_2^2\cos(2\delta_1-2\delta_2)-\frac{1}{8\omega_1}\beta_{15}\omega_2a_2^2\\ &\times\sin(2\delta_1-2\delta_2)+\frac{1}{4\omega_1}\beta_{16}\omega_2^2a_2^2\\ &-\frac{1}{8\omega_1}\beta_{16}\omega_2^2a_2^2\cos(2\delta_1-2\delta_2)+\frac{1}{8}\beta_{17}a_2^2\\ &\times\sin(2\delta_1-2\delta_2)+\frac{1}{8}\beta_{18}\omega_2a_2^2\cos(2\delta_1-2\delta_2)\\ &+\frac{1}{2\omega_1a_1}f\Omega^2\cos(\delta_1),\end{aligned} \tag{20.3}$$

$$\begin{aligned}\frac{d}{dt}\delta_2 = &\sigma_1+\omega_1-\omega_2+\frac{3}{8\omega_2}\beta_{21}a_2^2+\frac{1}{8}\beta_{23}\omega_2a_2^2\\ &+\frac{1}{4\omega_2}\beta_{24}a_1^2+\frac{1}{8\omega_2}\beta_{24}a_1^2\cos(2\delta_2-2\delta_1)\\ &-\frac{1}{8\omega_2}\beta_{25}\omega_1a_1^2\sin(2\delta_2-2\delta_1)+\frac{1}{4\omega_2}\beta_{26}\omega_1^2a_1^2\\ &-\frac{1}{8\omega_2}\beta_{26}\omega_1^2a_1^2\cos(2\delta_2-2\delta_1)+\frac{1}{8}\beta_{27}a_1^2\\ &\times\sin(2\delta_2-2\delta_1)+\frac{1}{8}\beta_{28}\omega_1a_1^2\cos(2\delta_2-2\delta_1)\\ &+\frac{1}{2\omega_2a_2}f\Omega^2\sin(\delta_2).\end{aligned} \tag{20.4}$$

where,

$$\delta_1 = \sigma_1t-\phi_1, \quad \delta_2 = \sigma_1t-\sigma_2t-\phi_2, \ \dot{\delta}_1 = \sigma_1-\dot{\phi}_1,$$
$$\dot{\delta}_2 = \sigma_1-\sigma_2-\dot{\phi}_2. \tag{21}$$

Substituting $F_1(T_1) = \frac{1}{2}a_1e^{i\phi_1}$ and $F_2(T_1) = \frac{1}{2}a_2e^{i\phi_2}$ into the first term of Eqs (17) taking into account Eqs. (19) and (21), we get the following periodic solutions of Eqs. (8) and (12):

$$u(t) = \frac{a_1}{2}e^{i(\omega_1t+\phi_1)}+\frac{a_1}{2}e^{-i(\omega_1t+\phi_1)} = a_1\cos(\Omega t-\delta_1), \tag{22.1}$$

$$v(t) = \frac{a_2}{2}e^{i(\omega_2t+\phi_2)}+\frac{a_2}{2}e^{-i(\omega_2t+\phi_2)} = a_2\cos(\Omega t-\delta_2) \tag{22.2}$$

where a_1 and a_2 as clear from Eqs (22) represent the dimensionless oscillation amplitudes of the 6-pole Rotor-AMBs in X and $y-$ directions, respectively, δ_1 and δ_2 denote the corresponding phase-angles. It is worth to mention that the oscillation amplitudes (i.e. a_1, a_2) and the corresponding phase angles (i.e. δ_1, δ_2) are governed by the first-order nonlinear averaged equations given in Eqs. (20).

IV. BIFURCATION DIAGRAMS AND SENSITIVITY INVESTIGATION

The oscillatory behaviors of the 6-pole Rotor-AMBs under the proposed control strategies are explored in this section.

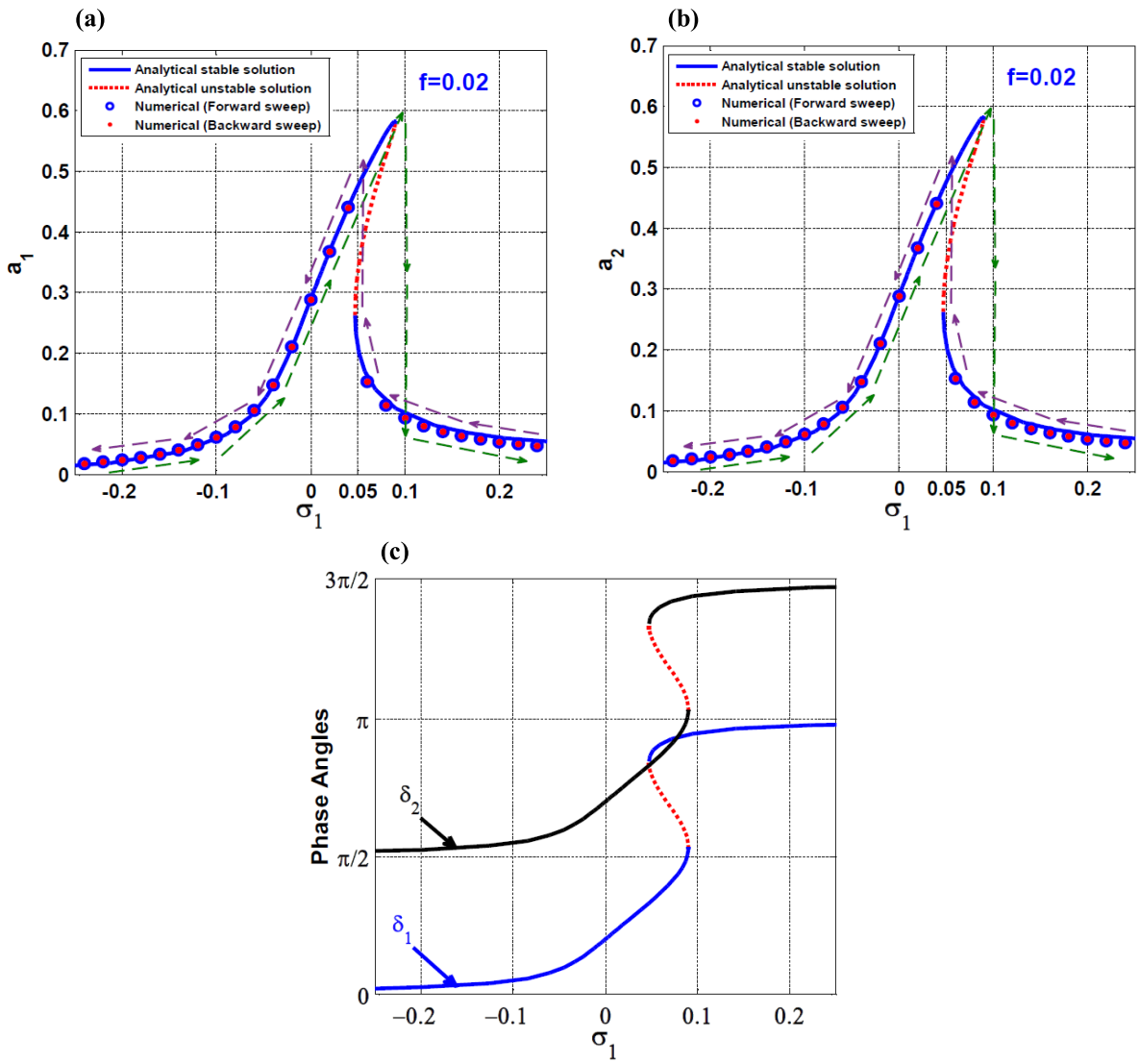

FIGURE 2. The system spinning-speed response-curve under radial control method at $f = 0.02$: (a) oscillation amplitude in $u-$direction, (b) oscillation amplitude in $v-$direction, and (c) phase angles of the two motions.

Setting $\dot{a}_j = \dot{\delta}_j = 0\,(j = 1, 2)$ into Eqs (20) leads to four nonlinear algebraic equations that govern the steady-state oscillation amplitudes and the modified phases of the considered system. By solving the resulting nonlinear algebraic equations numerically using the predictor-corrector continuation algorithm, one can investigate the system's sensitivity to the different control parameters. Moreover, the stability of the obtained solutions can be checked via investigating the eigenvalues of the **Jacobian-Matrix** of the right-hand side of Eqs (20). The efficiency of the proposed control methods in mitigating the system lateral oscillations is explored via plotting the system oscillation amplitudes (a_1, a_2) versus the different system parameters. According to Eqs (22), Rotor-AMBs can perform forward whirling motion if $\delta_2 > \delta_1$, while the system exhibits backward whirling motion for $\delta_2 < \delta_1$. Moreover, the rotating disk executes oscillations along a straight line when $\delta_2 = \delta_1$. Therefore, plotting the phase-angles (δ_1, δ_2) versus one of the system parameters makes us able to determine the whirling direction. In sections *IV-A* and *IV-B*, all bifurcation diagrams are obtained by solving the averaged equations given in (20) when $\dot{a}_1 = \dot{a}_2 = \dot{\delta}_1 = \dot{\delta}_2 = 0$ via utilizing one of the system parameters as a bifurcation control parameter. The solid lines refer to the stable solution, while the dotted lines represent the unstable solution.

A. RADIAL CONTROL STRATEGY

This section is intended to discuss the lateral vibrations of the 6-pole Rotor-AMBs under the radial control strategies. The following bifurcation diagrams are obtained via solving Eqs. (20) at $\dot{a}_1 = \dot{a}_2 = \dot{\delta}_1 = \dot{\delta}_2 = 0$ with adopting the system parameters values: $p = 1.1$, $d = 0.005$,

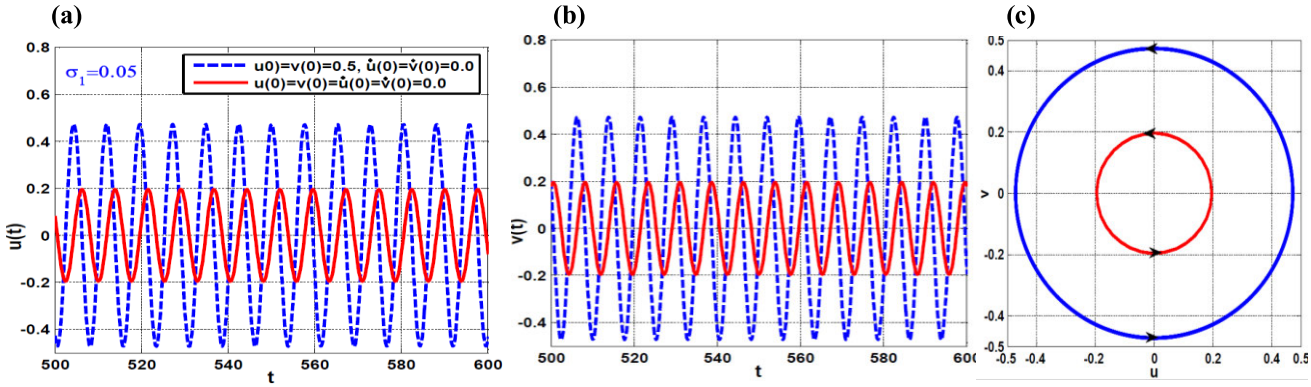

FIGURE 3. The system temporal oscillations according to Fig. 2 at $\sigma_1 = 0.05$ at two different initial conditions: (a, b) the oscillation amplitudes in u and $v-$directions, and (c) the steady-state whirling orbits.

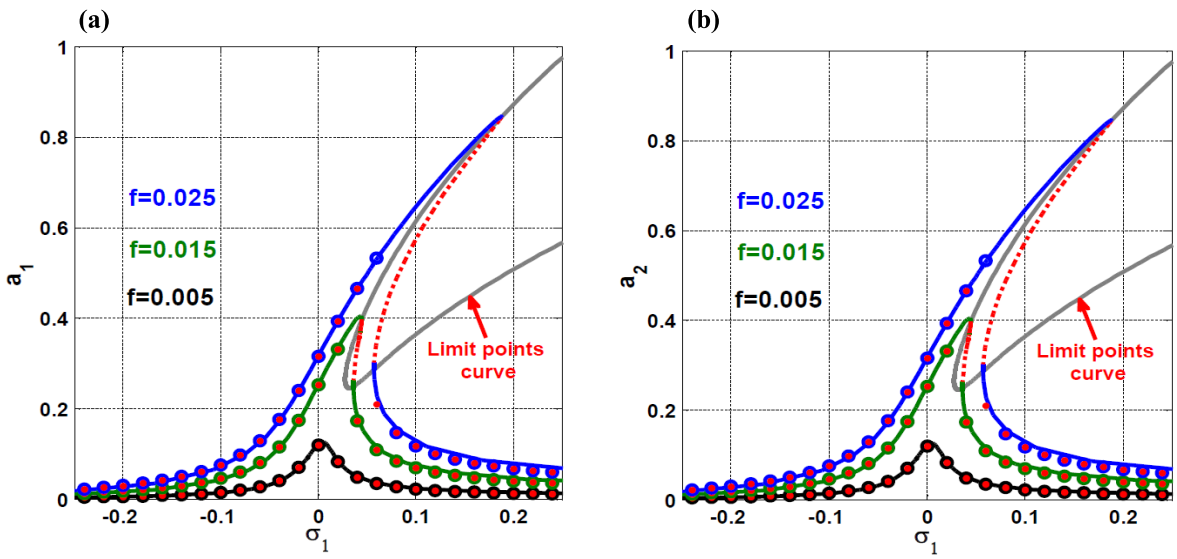

FIGURE 4. The system spinning-speed response-curve under radial control method at different levels of the disk eccentricity: (a) oscillation amplitude in $u-$direction, (b) oscillation amplitude in $v-$direction.

$\mu = 0.001, f = 0.02$, $\Omega = \omega_1 + \sigma_1, \mu_1 = \mu_2 = \mu + 6d, \omega_1 = \omega_2 = \sqrt{6(p-1)}, \beta_{11} = \beta_{21} = 9 - \frac{27}{2}p + \frac{9}{2}p^2, \beta_{12} = \beta_{22} = 9pd - \frac{27}{2}d, \beta_{13} = \beta_{23} = \frac{9}{2}d^2, \beta_{14} = \beta_{24} = \frac{9}{2}\left(2 - 3p + p^2\right), \beta_{15} = \beta_{25} = 6pd - 9d, \beta_{16} = \beta_{26} = \frac{3}{2}d^2, \beta_{17} = \beta_{27} = 3pd - \frac{9}{2}d, \beta_{18} = \beta_{28} = 3d^2$, unless otherwise is mentioned in [4]–[6]. As the detuning parameter σ_1 in Eq. (19) defines the closeness of the disk spinning-speed Ω to the system natural frequency $\omega_1 = \omega_2$. Accordingly, σ_1 is used as a bifurcation control parameter to show the influence of the spinning-speed variations on the system dynamical behaviors. Fig. 2 illustrates the 6-pole Rotor-AMBs spinning-speed response curves for both the oscillation amplitudes and the phase angles at the disk-eccentricity $f = 0.02$. Fig. 2a and 2b show the symmetric oscillations of the system in both in u and $v-$directions, which means that the rotating disk exhibits circular whirling motion under this control strategy at any disk spinning-speed. Moreover, Fig. 2c illustrates that the phase angle δ_2 is always greater than δ_1 (i.e. $\delta_2 > \delta_1$), which means that the rotating disk performs forward whirling motion. According to Fig. 2, the 6-pole Rotor-AMBs under the radial control strategy can perform circular forward whirling motions only for any spinning speed for the rotating disk. Fig. 2 also depicts the inherent system nonlinearities due to the electromagnetic coupling, where there is a spinning-speed interval at which the system can exhibit one of two stable oscillation amplitudes depending on the initial conditions.

It is worth to mention that the solutions of the dimensionless equations of motions (i.e. Eqs (8) or (12)) are $u(t) = a_1\cos(\Omega t - \delta_1)$ and $v(t) = a_2\cos(\Omega t - \delta_2)$ as given in Eqs (22). Also, the relations between the dimensionless displacements $(u(t), v(t))$ and the real displacements $(x(t), y(t))$ of the considered system are given by $u(t) = \frac{x(t)}{s_0}, v(t) = \frac{y(t)}{s_0}$, where s_0 is the air-gap size of the real system. Accordingly, if we supposed that the real vibration amplitudes are a_{1R} and a_{2R}. Then, the relations between the dimensionless vibration

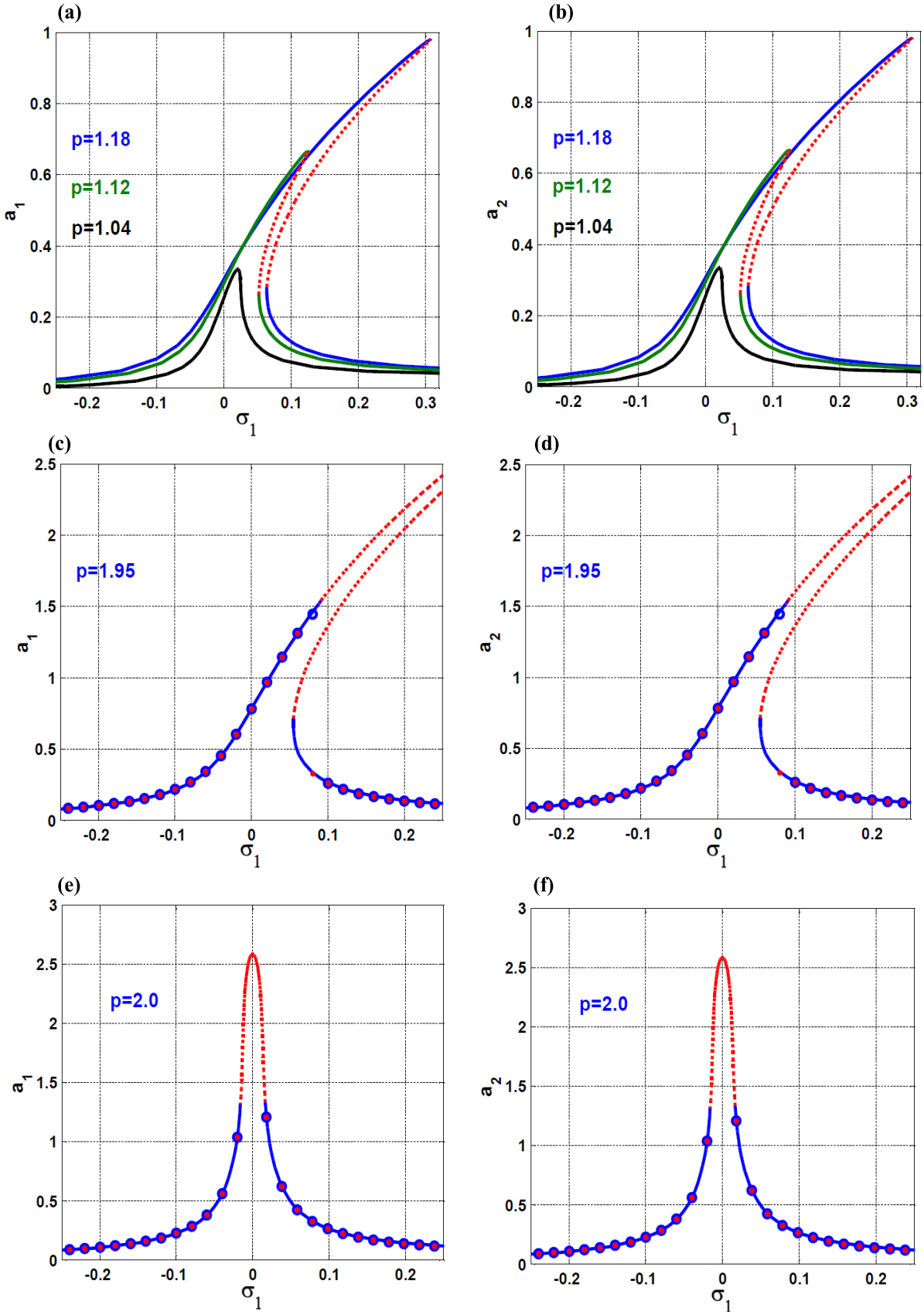

FIGURE 5. The system spinning-speed response-curve under radial control method at different values of the proportional control gain: (a) oscillation amplitude in u−direction, (b) oscillation amplitude in v−direction.

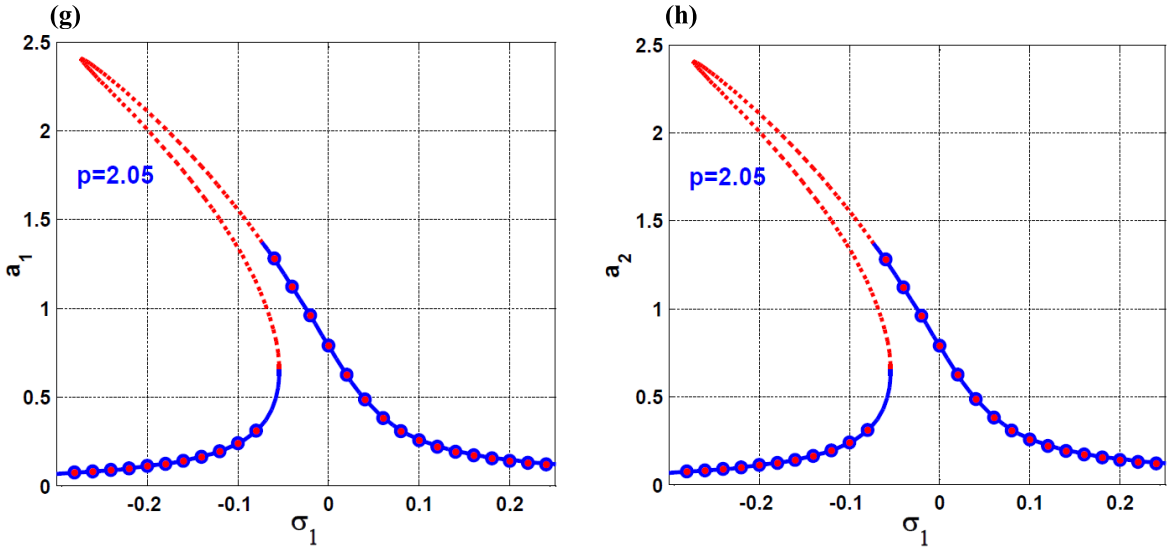

FIGURE 5. *(Continued.)* **The system spinning-speed response-curve under radial control method at different values of the proportional control gain: (a) oscillation amplitude in $u-$direction, (b) oscillation amplitude in $v-$direction.**

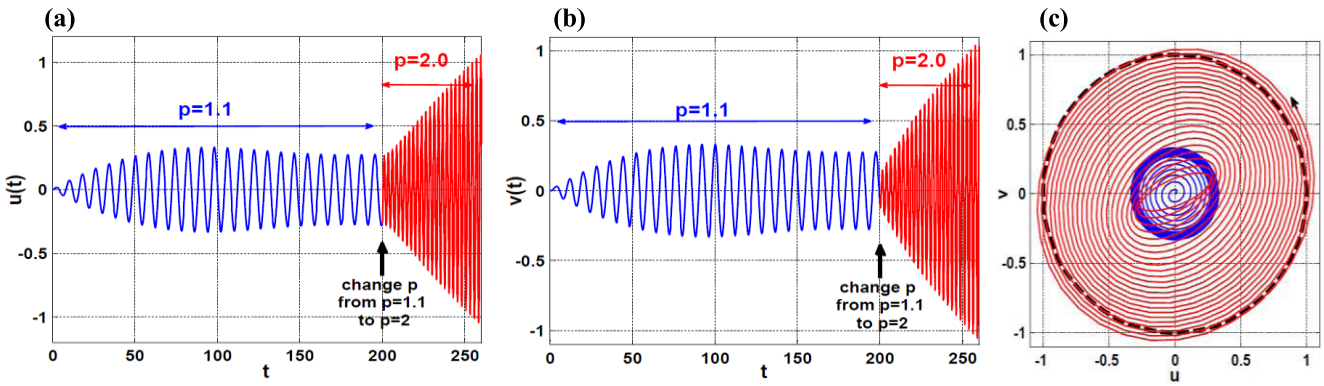

FIGURE 6. **The effect of online switching the proportional control gain from $p = 1.1$ to $p = 2.0$ on the system oscillation amplitudes according to Fig.5 at $\sigma_1 = 0.0$: (a, b) the oscillation amplitudes in u and $v-$directions, and (c) phase plane.**

amplitudes (a_1, a_2) and the real vibration amplitudes (a_{1R}, a_{2R}) are given by $a_1 = \frac{a_{1R}}{s_0}$, $a_2 = \frac{a_{2R}}{s_0}$. This means that as $a_1 < 1$ and $a_2 < 1$, the real system oscillation amplitudes do not exceed the air gap-size. Therefore, to guarantees the system operation in the safe mode without the occurrence of the rub/impact forces between the rotating disk and the stator, the oscillation amplitudes (a_1 and a_2) should be less than unity. According to Fig. 2 at $\sigma_1 = 0.05$, the system temporal oscillations and the corresponding steady-state whirling orbit are simulated in Fig. 3 via solving Eqs (8) numerically using **ODE45 Matlab solver** at $\Omega = \omega_1 + 0.05$. As Fig. 2 confirms the existence of two stable vibration amplitudes at $\sigma_1 = 0.05$, two different initial conditions are tried for solving Eqs (8) numerically. It is clear from Fig. 3 that the system is sensitive to the initial conditions at this value of the disk spinning-speed, where the system exhibits two different oscillation amplitudes depending on the initial conditions. Moreover, the whirling orbits, shows that the system can perform circular forward whirling motions only. The system oscillation amplitudes at different values of the disk eccentricity f are investigated in Fig. 4. The figure shows that the system vibration amplitudes are a monotonic increasing function of the disk eccentricity. Moreover, the hardening spring characteristic dominates the system response for large values of the rotating disk eccentricity, where jump phenomenon and multivalued solutions appear. It is important to notice that the relation between the dimensionless disk eccentricity f and its real value E is given as $f = \frac{E}{s_0}$, where s_0 is the air-gap size. Accordingly, when $f = 0.02$ this means that the real disk eccentricity is 0.02 of the air-gap size s_0 of the system.

Going back to the dimensionless parameters given before Eqs (8), we found that $p = \frac{s_0}{I_0}k_1$ and $d = \frac{s_0\omega_n}{I_0}k_2$, where s_0, I_0 and $\omega_n = \sqrt{\frac{\mu_0 I_0^2 N^2 A cos(\varphi)}{4ms_0^3}}$ are constants that depending on the physical structure of the Rotor-AMBs and its size. Accordingly, we can consider that p represents the dimensionless proportional control gain, and d denotes the dimensionless derivative control gain. The influence of both the

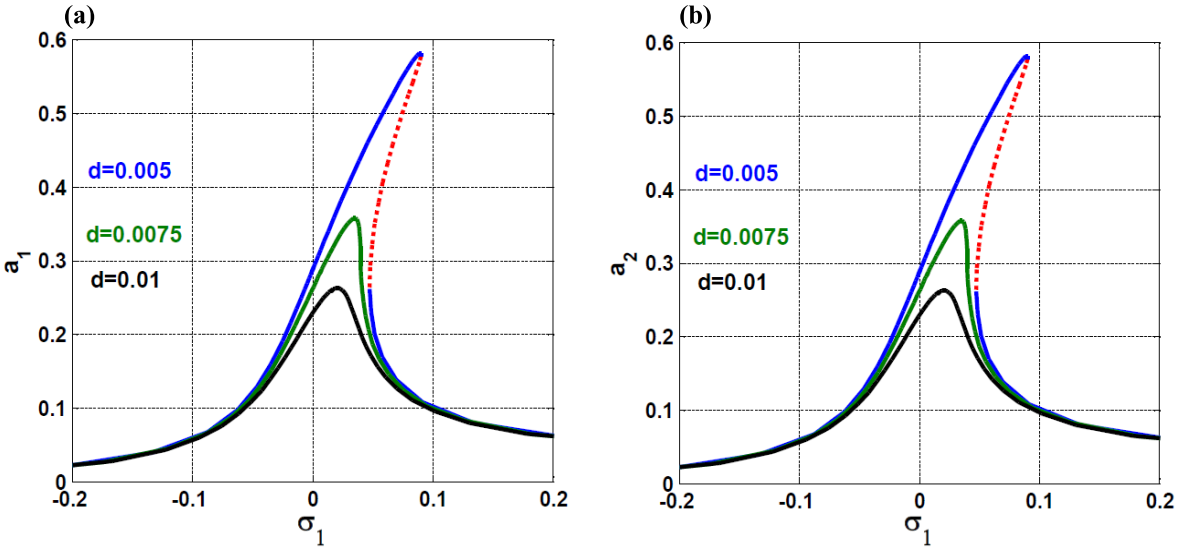

FIGURE 7. The system spinning-speed response-curve under the radial control method at different values of the derivative control gain: (a) oscillation amplitude in $u-$direction, (b) oscillation amplitude in $v-$direction.

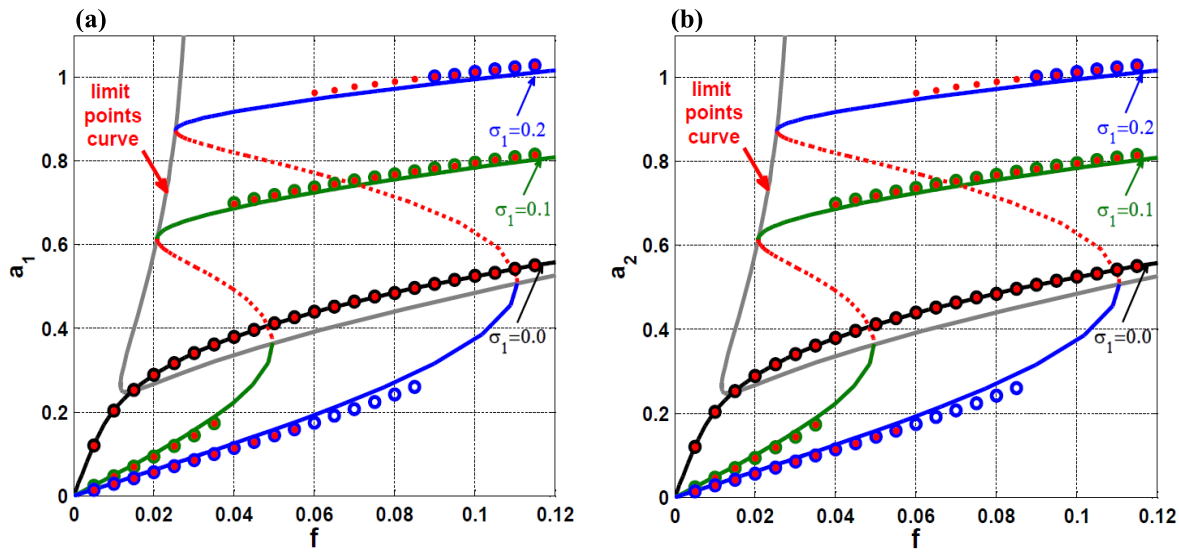

FIGURE 8. The system eccentricity response-curve under the radial control method at different values of the disk spinning-speed: (a) oscillation amplitude in $u-$direction, (b) oscillation amplitude in $v-$direction.

proportional and derivative control gains on the system dynamical behaviors are investigated in Figs. 5 and 6, respectively. The effect of increasing the proportional control gain p on the 6-pole Rotor-AMBs lateral vibrations is showed in Fig. 5. Generally, the figure shows that increasing the proportional control gains increases the system oscillation amplitudes and can change the system restoring force form hardening spring characteristics as in Figs. 5a, 5b, 5c, 5d to softening one as in Figs. 5g, 5h. Moreover, the system can exhibit unbounded response as Figs. 5e, and 5f imply at some spinning-speed values. Figs. 5a and 5b illustrate that as long as $p \leq 1.18$, the system can operate in the safe mode where the oscillation amplitudes $a_1 < 1$ and $a_2 < 1$. Besides, it is clear that minimizing the proportional control gain magnitude improves the system dynamical behaviors, but there is a specific lower limit for p to guarantee the system stability. To guarantee the system stability, the system natural frequencies $\omega_1 = \omega_2 = \sqrt{6(p-1)}$ should be positive values (i.e. $\sqrt{6(p-1)} > 0$). Therefore, the proportional control again should be greater than unity (i.e. $p > 1$). Accordingly, the optimal values of the proportional control gain should be within the range of $1 < p \leq 1.18$. Fig. 6 simulates numerically the effect of ***online switching*** the proportional control gain from $p = 1.1$ to $p = 2.0$ when $t = 200$ at the perfect tuning (i.e. $\sigma_1 = 0.0$) on the 6-pole Rotor-AMBs lateral oscillations. The figure shows that the system exhibits

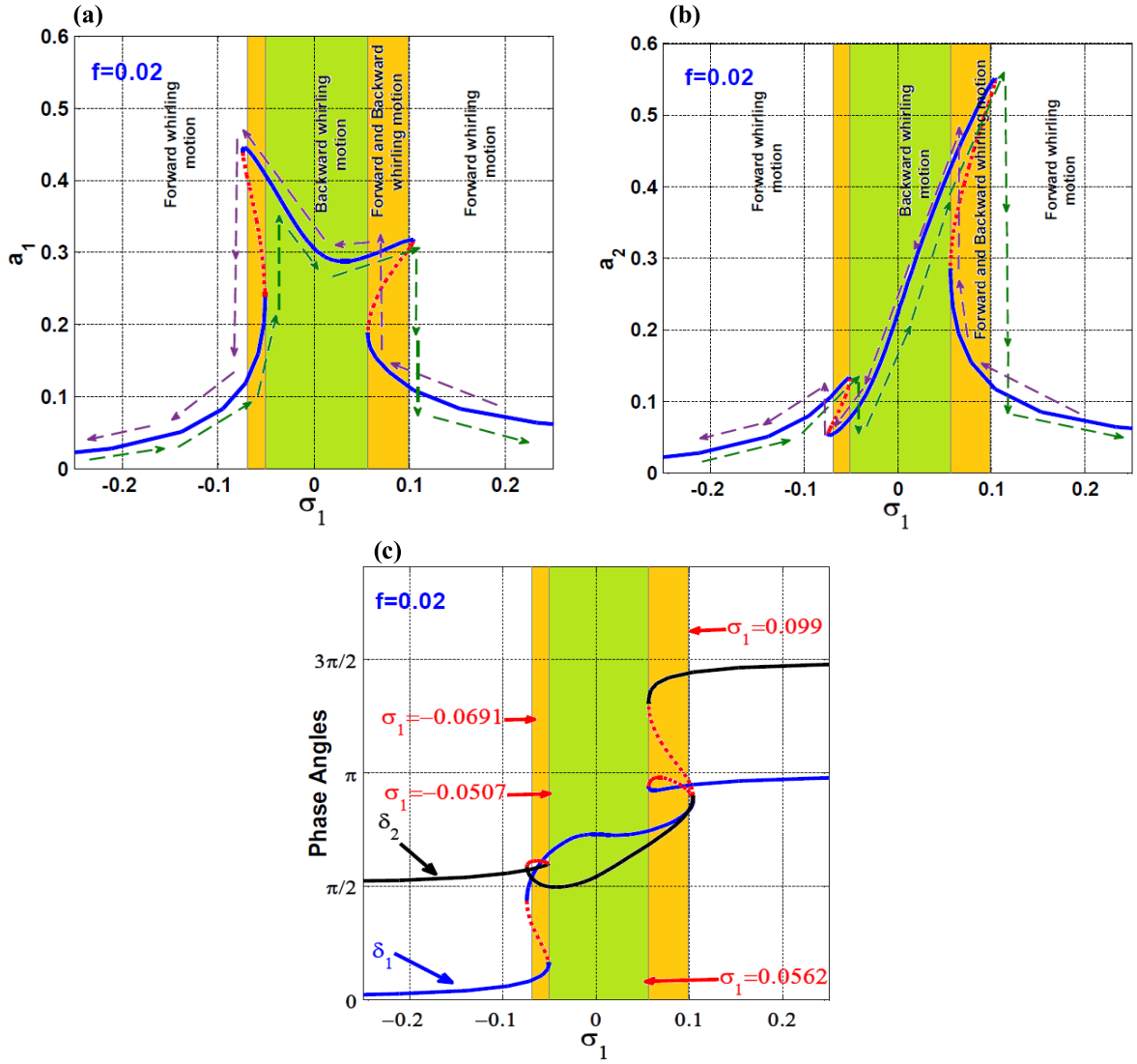

FIGURE 9. The system spinning-speed response-curve under cartesian control method at $f = 0.02$: (a) oscillation amplitude in $u-$direction, (b) oscillation amplitude in $v-$direction, and (c) phase angles of the two motions.

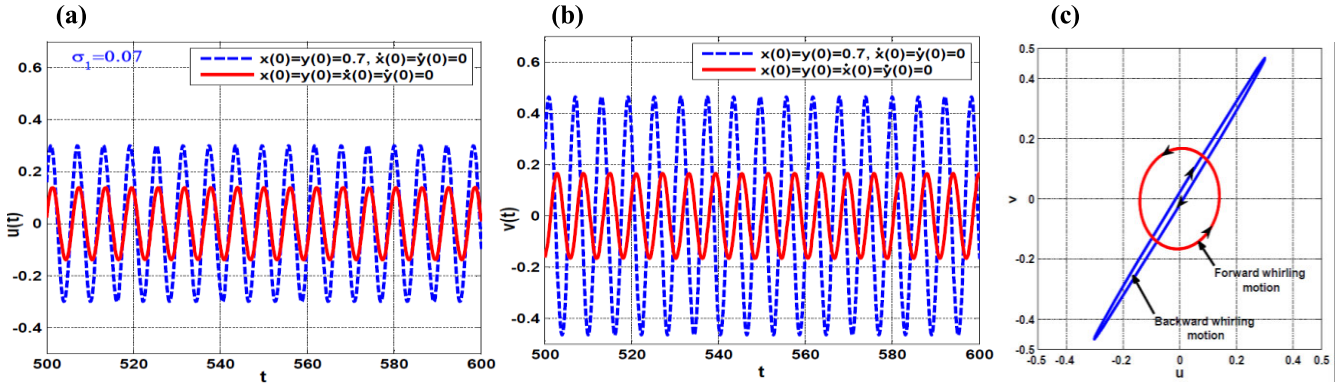

FIGURE 10. The system temporal oscillations according to Fig.9 at $\sigma_1 = 0.07$ at two different initial conditions: (a, b) oscillation amplitudes in u and $v-$directions, and (c) the steady-state whirling orbits.

stable lateral oscillation amplitudes as long as $p = 1.1$, but when the proportional control gain is increased abruptly to $p = 2.0$ a growth for the vibration amplitudes is noticed leading to rub/impact forces occurrence and system instability as Figs. 5e and 5f confirm. The influence of increasing the derivative control gain of the 6-pole Rotor-AMBs oscillations

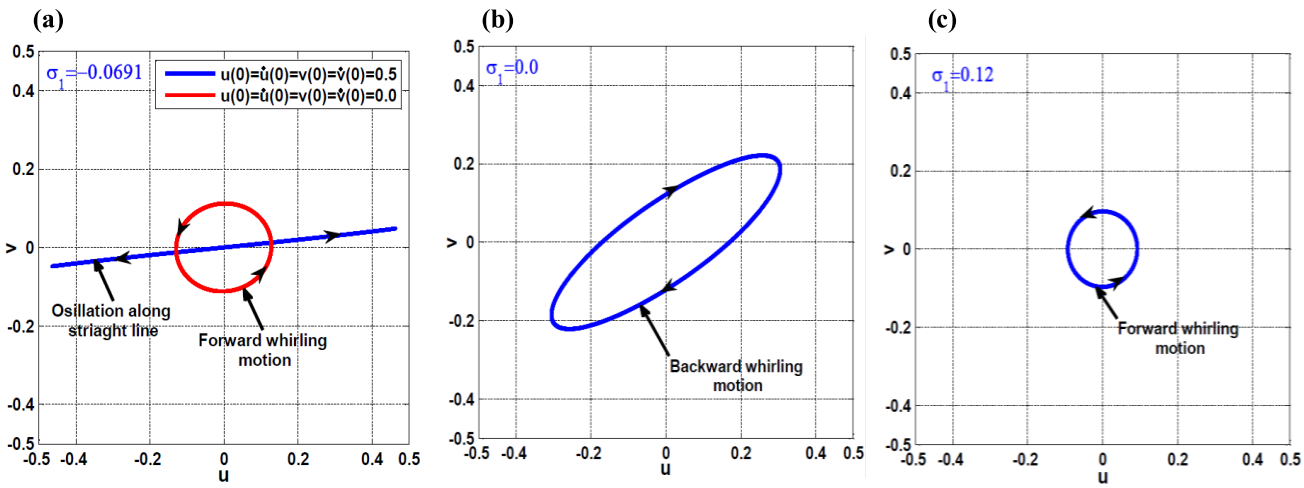

FIGURE 11. The system whirling modes according to Fig.9: (a) oscillation along a straight line or whirling forward at $\sigma_1 = -0.0691$, (b) backward whirling mode $\sigma_1 = 0.0$, and (c) forward whirling mode $\sigma_1 = 0.12$.

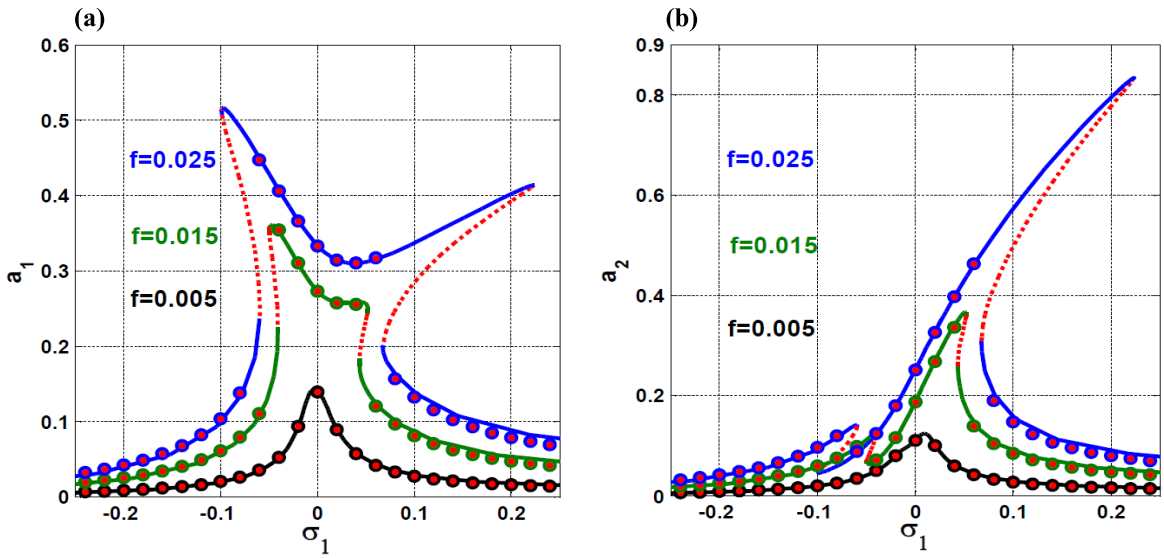

FIGURE 12. The system spinning-speed response-curve under the cartesian control method at different levels of the disk eccentricity: (a) oscillation amplitude in $u-$direction, (b) oscillation amplitude in $v-$direction.

is illustrated in Fig. 7. The figure illustrates that increasing d, increases the system linear damping coefficients, which ultimately decreases the system oscillation amplitudes. However, the derivative control gain d is included in the most nonlinear terms β_{ij}, $(i = 1, 2, j = 1, 2, \ldots, 8)$, increasing its magnitude has not any influence on the nonlinear dynamical behavior of the system that is not the case of the proportional control gain. The oscillatory motion of the system subjected to large values of the disk eccentricity is presented in Fig. 8. The system eccentricity is utilized as a bifurcation control parameter to explore the system vibration amplitudes at different values of the disk spinning-speed σ_1. The figure shows that the system oscillation amplitudes are stable from the theoretical point of view for any value of the disk eccentricity. However, it is noticed that the oscillation amplitudes are greater than unity for some values of the disk eccentricity that leading to the rub/impact forces and system instability.

B. CARTESIAN CONTROL STRATEGY

The dynamical behaviors of the considered system under cartesian control strategy is investigated within this section. According to the parameters definitions given after Eqs (12), we have $\mu_1 = \mu + 4d(\gamma + 1)$, $\mu_2 = \mu + 4\sqrt{3}\, d$, $\omega_1 = \sqrt{4p(\gamma + 1) - 6}$, $\omega_2 = \sqrt{4\sqrt{3}\, p - 6}$. So, to get symmetric linear damping coefficients (i.e. $\mu_1 = \mu_2$) and natural frequencies (i.e. $\omega_1 = \omega_2$), the dimensionless parameter γ should be equal to $\sqrt{3} - 1$. Therefore, the following bifurcation diagrams are obtained via solving Eqs. (20) at $\dot{a}_1 = \dot{a}_2 = \dot{\delta}_1 = \dot{\delta}_2 = 0$ with adopting the system

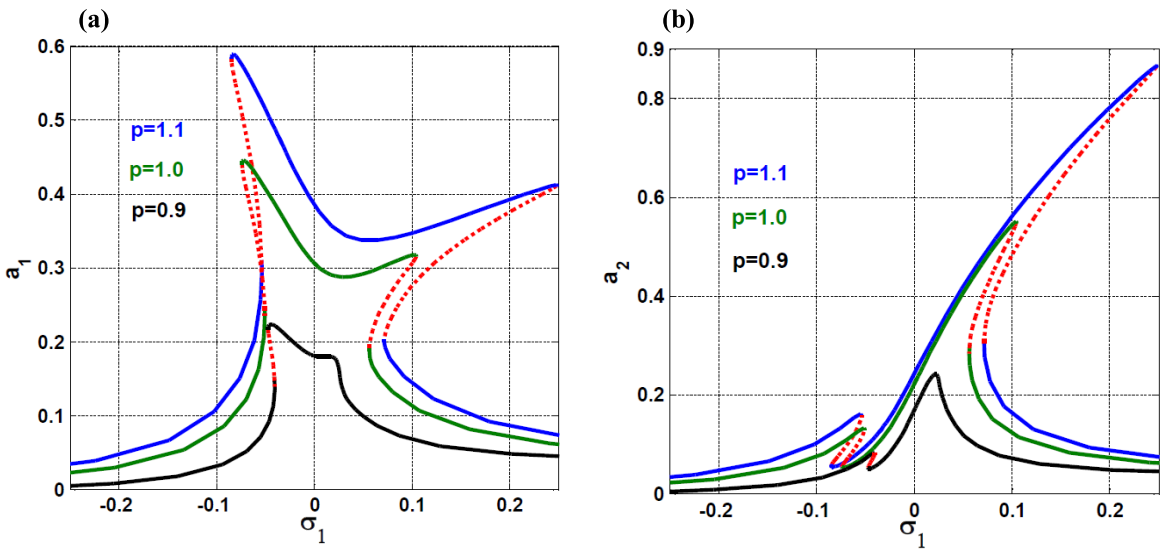

FIGURE 13. The system spinning-speed response-curve under cartesian control method at different values of the proportional control gain: (a) oscillation amplitude in $u-$direction, (b) oscillation amplitude in $v-$direction.

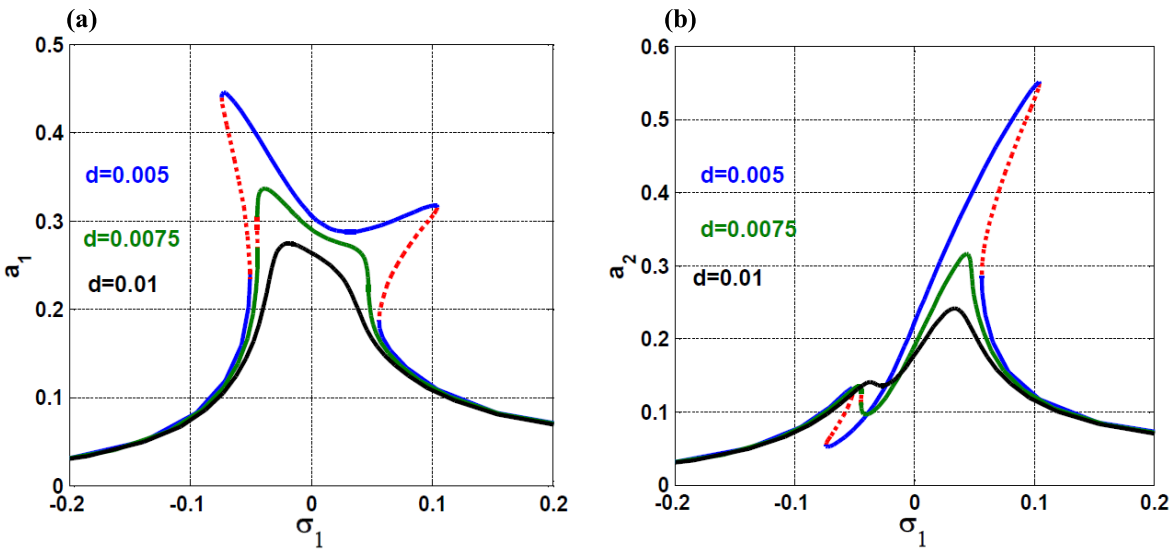

FIGURE 14. The system spinning-speed response-curve under cartesian control method at different values of the derivative control gain: (a) oscillation amplitude in $u-$direction, (b) oscillation amplitude in $v-$direction.

parameters values: $p = 1.0$, $d = 0.005$, $\mu = 0.001$, $f = 0.02$, $\Omega = \omega_1 + \sigma_1$, $\gamma = \sqrt{3} - 1$, $\mu_1 = \mu + 4d(\gamma + 1)$, $\mu_2 = \mu + 4\sqrt{3}\, d$, $\omega_1 = \sqrt{4p(\gamma + 1) - 6}$, $\omega_2 = \sqrt{4\sqrt{3}\, p - 6}$, $\beta_{11} = 9 - 3p(\gamma + 4) + 4p^2(\gamma^2 + 1)$, $\beta_{21} = 9 + 6p^2 - 3^{\frac{5}{2}} p$, $\beta_{12} = 4pd(2 + \gamma^2) - 6d(2 + \gamma)$, $\beta_{22} = 12pd - 3^{\frac{5}{2}} d$, $\beta_{13} = 2d^2(2 + \gamma^2)$, $\beta_{23} = 16d^2$, $\beta_{14} = \left(4\sqrt{3}\gamma + 2\right)p^2 - \left(9\gamma + 6\sqrt{3}\right)p + 9$, $\beta_{24} = \left(6\gamma + 4\sqrt{3}\right)\gamma p^2 - \left(18\gamma + 3\sqrt{3}\right)p + 9$, $\beta_{15} = 4\left(\sqrt{3}\gamma + 1\right)pd - 6\sqrt{3}\, d$, $\beta_{25} = 4\left(3\gamma + \sqrt{3}\right)\gamma pd - 18\gamma d$, $\beta_{16} = 2d^2$, $\beta_{26} = 6\gamma^2 d^2$, $\beta_{17} = \left(4\sqrt{3}\, p - 9\right)\gamma d$, $\beta_{27} = \left(4\sqrt{3}\gamma p - 3\sqrt{3}\right)d$, and $\beta_{18} = \beta_{28} = 4\sqrt{3}\gamma d^2$ unless otherwise is mentioned in [4]–[6]. Fig. 9 illustrates the system lateral vibration amplitudes and the corresponding phase angles under the cartesian control strategy. It is clear from Figs. 9a and 9b that the oscillation amplitudes in u and $v-$directions are asymmetric. Moreover, the system can vibrate with different whirling modes depending on the disk spinning-speed and its initial conditions as Fig. 9c implies. The different whirling modes (either forward, backward, both forward and backward, or along a straight line) are illustrated on Figs. 9a and 9b with different colored regions depending on the relation between the phase angles δ_1 and δ_2 in Fig. 9c. In additions, the figure shows that the system may be

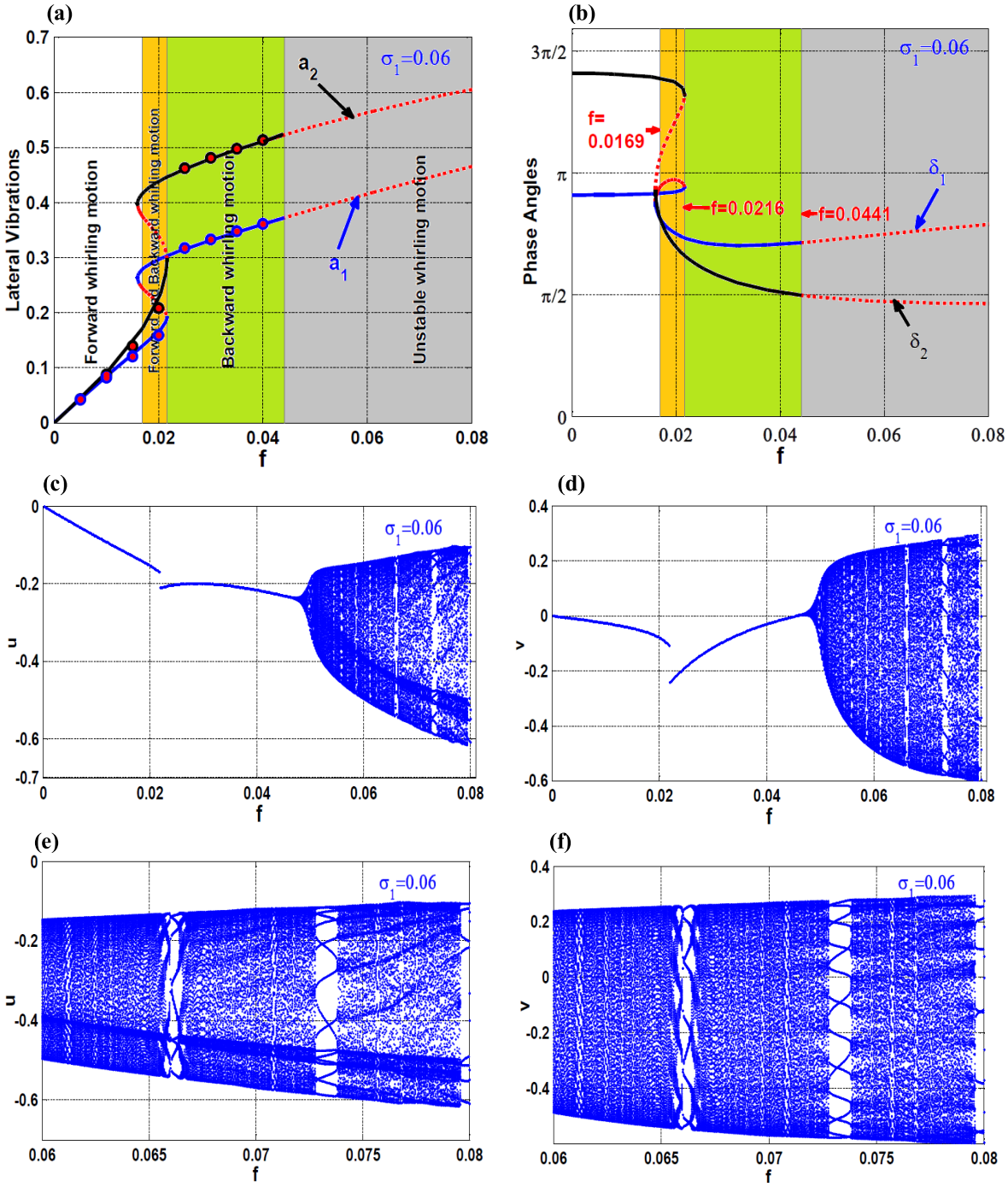

FIGURE 15. The system eccentricity response-curve under cartesian control method when the disk spinning-speed $\Omega = \omega_1 + 0.06$: (a) oscillation amplitude in u and $v-$direction, (b) the corresponding phase angles, (c, d) the system bifurcation diagrams, and (e, f) enlarging of Figs (c, d).

subjected to two consecutive jump phenomenon while the disk spinning-speed crossing the critical speed. Numerical simulation for the lateral vibrations of the 6-pole Rotor-AMBs according to Fig. 9 at $\sigma_1 = 0.07$ is presented in Fig. 10. Because of Figs. 9a and 9b imply that the system can respond with one of two stable oscillation amplitudes at $\sigma_1 = 0.07$, two different initial conditions are tried to solve the original differential equations(i.e. Eqs (12)) numerically. It is clear from Figs. 9 and 10 the excellent agreements between the analytical solutions given by the averaged equations (i.e. Eqs (20)) and the numerical results, where the system exhibits both forward and backward whirling motions at the same spinning speed (i.e. $\Omega = \omega_1 + \sigma_1 = 0.07$) depending on the initial conditions.

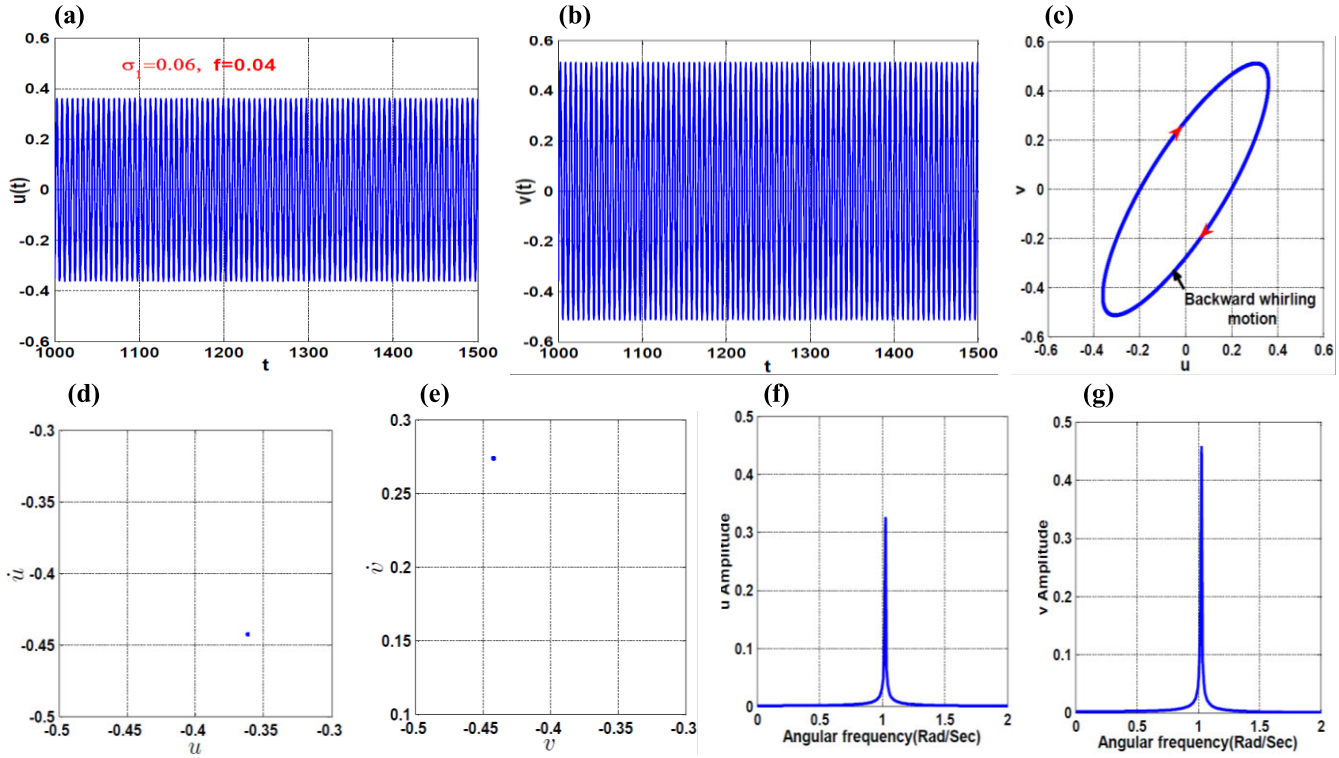

FIGURE 16. The system temporal oscillations according to Fig. 15 at $f = 0.04$: (a, b) oscillation amplitudes in u and $v-$directions, (c) the steady-state whirling orbit, (d, e) Poincare-map, and (f, g) frequency-spectrum.

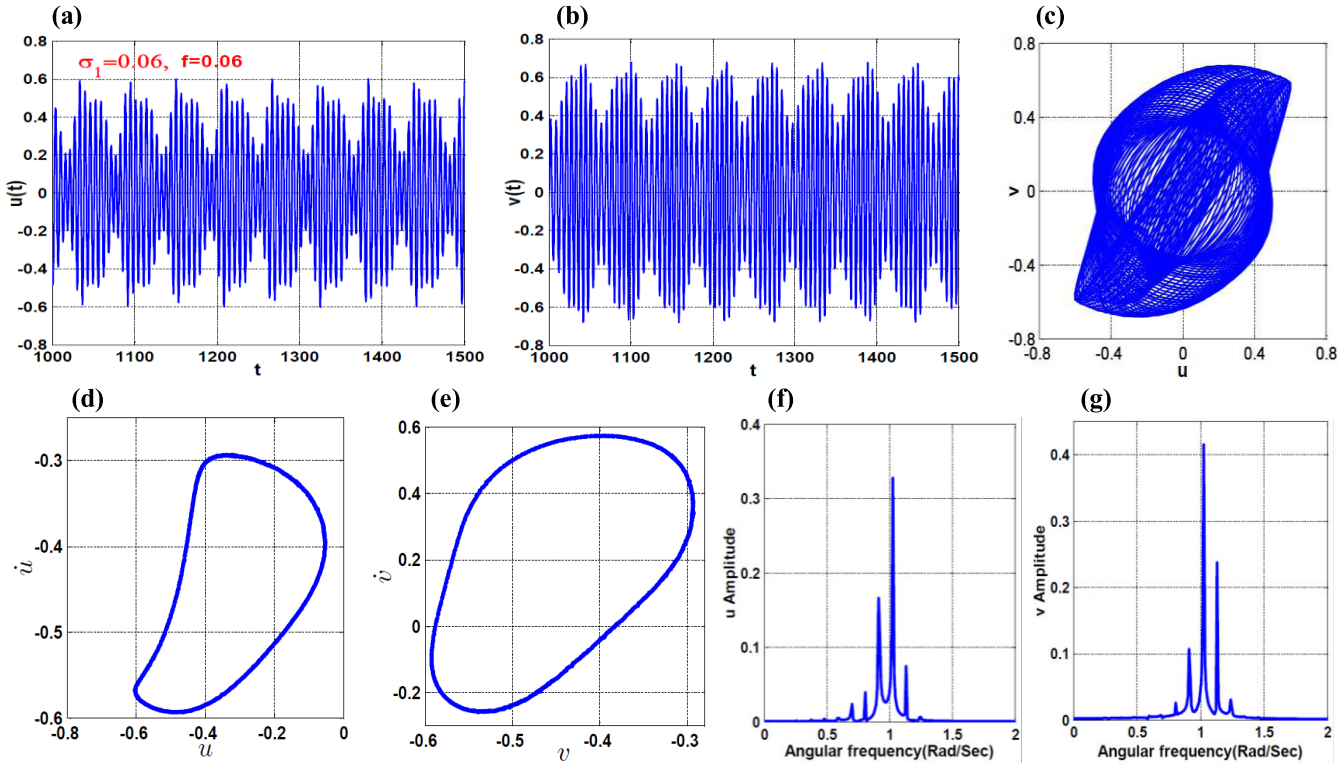

FIGURE 17. The system temporal oscillations according to Fig. 15 at $f = 0.06$: (a, b) oscillation amplitudes in u and $v-$directions, (c) the steady-state whirling orbit, (d, e) Poincare-map, and (f, g) frequency-spectrum.

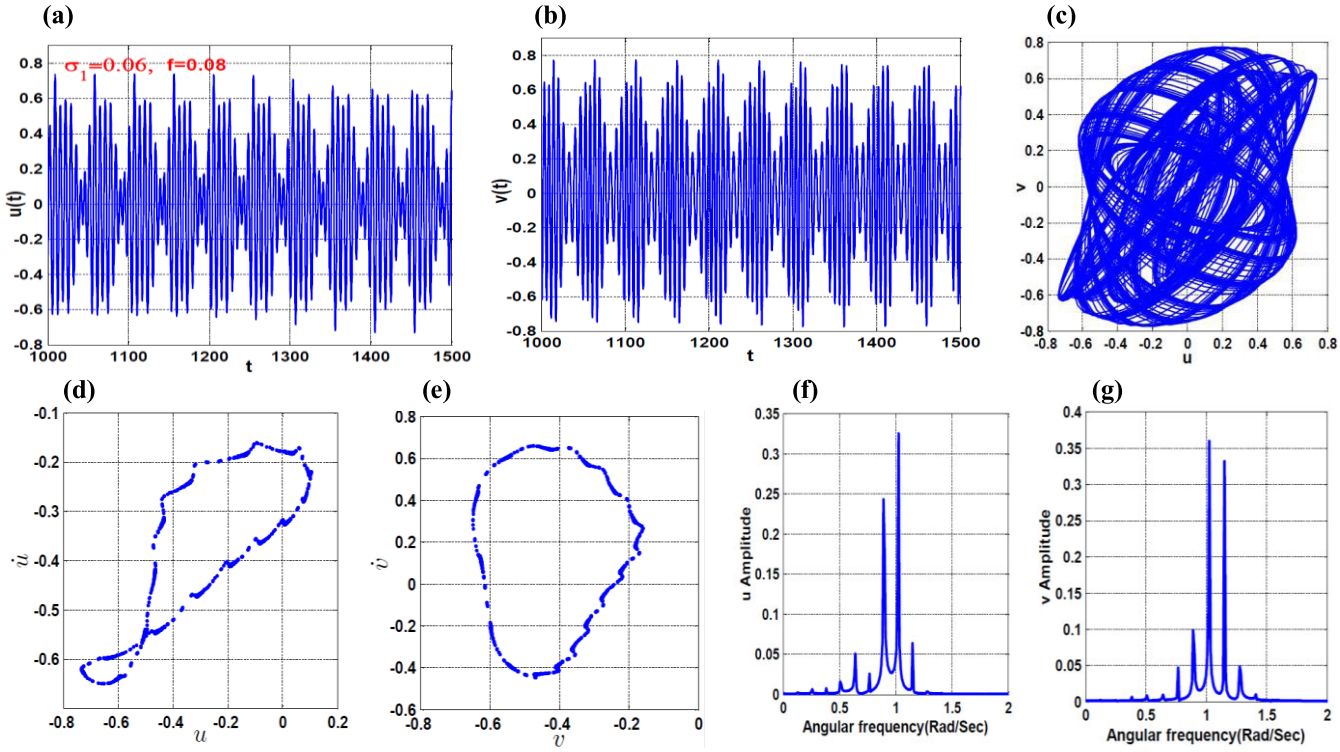

FIGURE 18. The system temporal oscillations according to Fig. 15 at $f = 0.08$: (a, b) oscillation amplitudes in u and $v-$directions, (c) the steady-state whirling orbit, (d, e) Poincare-map, and (f, g) frequency-spectrum.

Based on the relation between the phase angles δ_1 and δ_2 that illustrated in Fig. 9c, different whirling orbits are obtained numerically to confirm the different whirling modes that can be exhibited by the considered system at the cartesian control strategy as shown in Fig. 11. The effect of increasing the disk eccentricity on Rotor-AMBs under the cartesian control method is illustrated in Fig. 12. The figure shows that the system responds as a linear one with symmetric oscillations in u and $v-$directions for small disk centricity (i.e. $f = 0.005$). Moreover, the nonlinearity due to the electromagnetic coupling dominates the system response for large values of the disk eccentricity, where the bistable solution, multi jump phenomenon, and different whirling modes can be e noticed. The influences of both the proportional and derivative control gains on the vibrational behaviors of the considered system are investigated in Figs. 13 and 14, respectively. Fig. 13 shows the system spinning-speed response curve at three different values of the proportional control gain. It clear from the figure that the increase of the proportional control gain widens the spinning-speed interval at which the system exhibits large oscillation amplitudes. However, the system can operate in the safe mode as long as $p \leq 1.1$, where the oscillation amplitudes $a_1 < 1$ and $a_2 < 1$. Moreover, it is clear that the minimization of the proportional control gain decreases the lateral vibrations of the system, but there is a constrain on the smallest possible value of p to guarantee system stability. The natural frequencies of the system under this control method should be positive values to guarantee the system stability (i.e. $\omega_1 = \omega_2 = \sqrt{4\sqrt{3}\,p - 6} > 0$). Therefore, the proportional control again should be greater than $\sqrt{3}/2$. Accordingly, the optimal values of the proportional control gain in the cartesian control method should be with the range $\frac{\sqrt{3}}{2} < p \leq 1.1$. The influence of increasing the derivative control gain on the 6-pole Rotor-AMBs oscillations is illustrated in Fig. 14. The figure illustrates that increasing the derivative gain increases the system linear damping coefficients, which ultimately decreases the system oscillation amplitudes.

The oscillatory behaviors of the considered system for a wide range of the disk eccentricity under the cartesian control method at three different values of the disk spinning-speed are explored in Figs. 15, 19, and 20. The system eccentricity response-curve for both the oscillation amplitudes and the corresponding phase-angles at disk spinning-speed $\Omega = \omega_1 + 0.06$ are illustrated in Figs. 15a and 15b, respectively. It clear from the figure that the system can oscillate with one of four whirling modes depending on the disk eccentricity magnitude, where the system may perform forward whirling motion only as long as $f < 0.0169$, but when $0.0169 < f < 0.0216$, the system exhibits either forward or backward whirling motion depending on the initial conditions. Moreover, the system can perform backward whirling motion only if the disk eccentricity belongs to the interval $]0.0216, 0.0441[$, but for $f > 0.0441$ the system loses its stability. To explore the nature of instability mode that occurs for $f > 0.0441$, the system bifurcation diagram is constructed as shown in Figs. 15c and 15d via solving Eqs (12) numerical for the same system parameter that used to obtain Fig. 15.

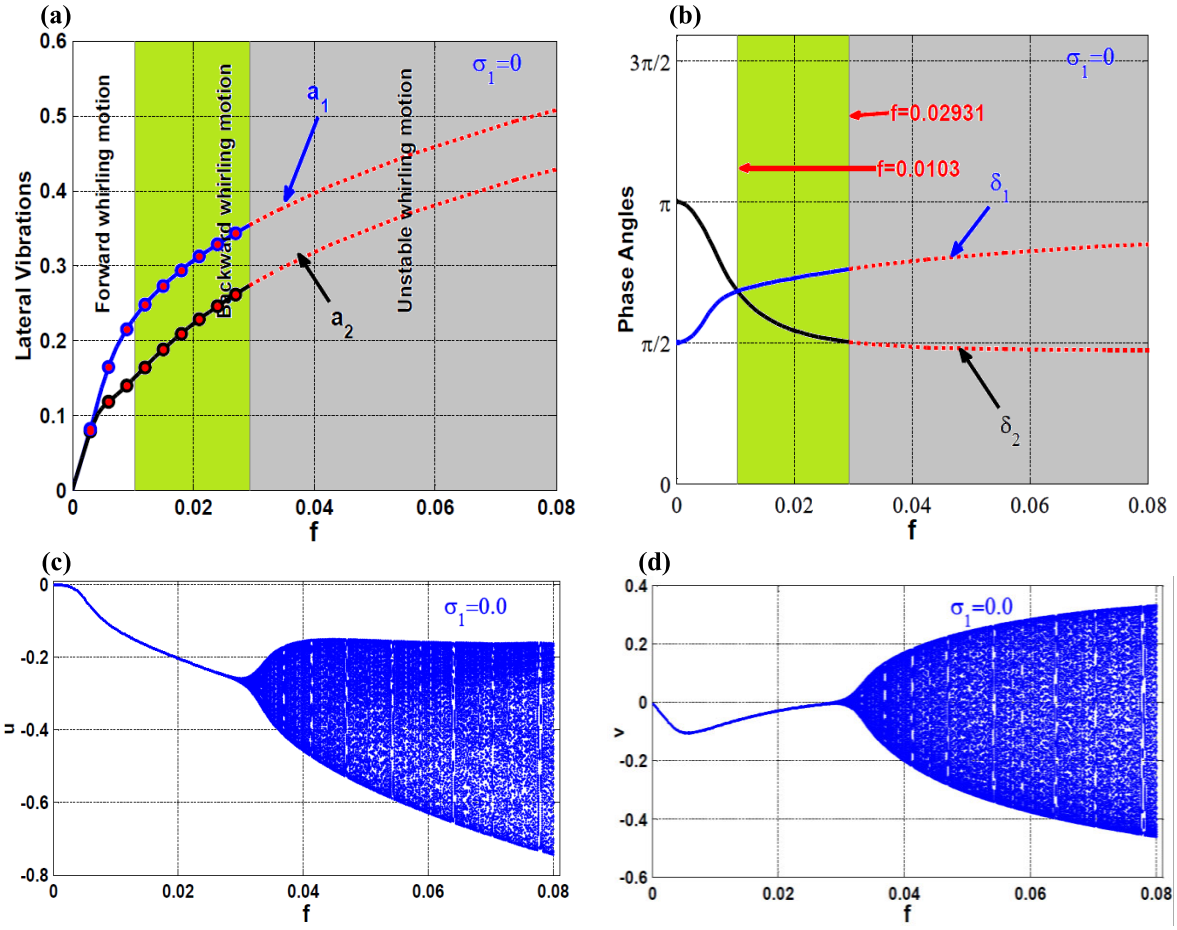

FIGURE 19. The system eccentricity response-curve under cartesian control method at the disk spinning-speed $\Omega = \omega_1 + 0.0$: (a) oscillation amplitude in u and $v-$direction, (b) the corresponding phase angles, (c, d) the system bifurcation diagrams.

By examining the obtained bifurcation diagrams, we can conclude that the system can execute bounded unstable periodic motions if $f > 0.0441$.

According to Fig. 15, numerical validations in terms of the steady-state temporal vibration, whirling orbit. Poincare map and frequency spectrum are presented in Figs. 16, 17, and 18, respectively. Fig. 16 simulates the system dynamics according to Fig. 15 when the disk eccentricity $f = 0.04$. It is clear from the figure that the system performs periodic motions in u and $v-$direction and can exhibit backward whirling motion only regardless of the system initial conditions that agrees in the excellent form the obtained analytical results in Figs. 15a and 15b. Figs. 17 and 18 show the system dynamics according to Fig. 15 when the disk eccentricity $f = 0.06$ and $f = 0.08$, respectively. It is clear from Poincare-maps and the frequency spectrum given in Figs. 17 and 18 that the system can execute quasi-periodic motions for $f > 0.0441$. Figs. 19 and 20 illustrate the system dynamical behaviors for a wide range of the disk eccentricity at the disk spinning speeds $\Omega = \omega_1 + 0.0$ and $\Omega = \omega_1 - 0.06$, respectively. Comparing Figs. 15, 19, and 20, we can conclude that increasing the disk eccentricity with fixing the spinning-speed constant can change the system whirling modes from one to another. However, if the disk eccentricity exceeds specific limit (that depends on the disk spinning-speed σ_1) the system periodic motion loses its stability via Hopf bifurcation leading to quasi-period oscillations. Accordingly, the effect of the proportional and derivative control gains on the stability margin for the disk eccentricity is investigated in term of $f - \sigma_1$ plane as shown in Fig. 21. Fig. 21a illustrates the effect of increasing the derivative control gain on the stability margin of the disk eccentricity for a wide range of the disk spinning-speed. The figure confirms that the stability margin widens as the derivative control gain is increased. Fig. 21b shows the effect of increasing the proportional control gain on the stability margin of the disk eccentricity for a wide range of the disk spinning-speed. It is found that as the proportional control gain is increased the stability margin is narrowed. Moreover, it is clear from Fig. 21 that the worst spinning-speed at which the system may lose its stability for small disk eccentricity is the system critical speed (i.e. when $\sigma_1 = 0.0$).

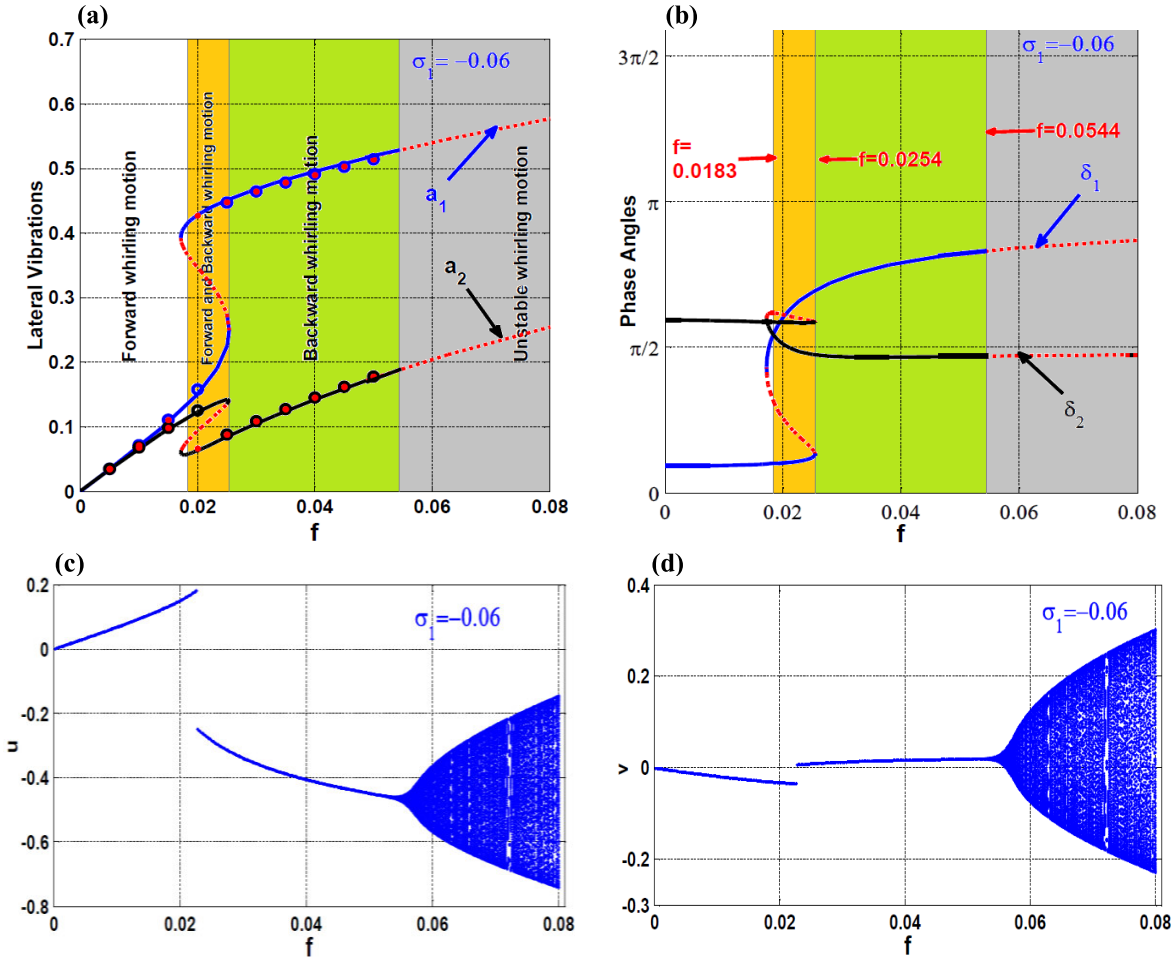

FIGURE 20. The system eccentricity response-curve under cartesian control method at the disk spinning-speed $\Omega = \omega_1 - 0.06$: (a) oscillation amplitude in u and $v-$direction, (b) the corresponding phase angles, (c, d) the system bifurcation diagrams.

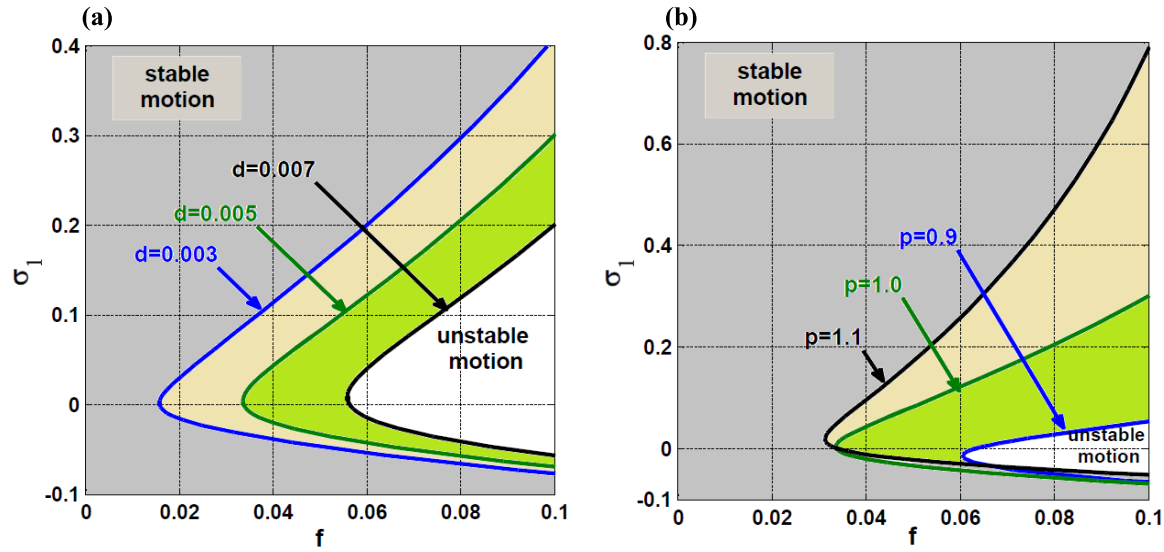

FIGURE 21. Stability chart in σ_1-f plane of the 6-pole Rotor-AMBs under cartesian control method: (a) effect of increasing d on the stability region, (b) effect of increasing p on the stability region.

C. RADIAL VERSUS CARTESIAN CONTROL STRATEGIES

This section presents a comparative study between the applied control strategies in terms of both efficiency in mitigating the system whirling motion and the robustness against the system instability. Figs. 22 and 23 compare the system dynamical behaviors under the applied control

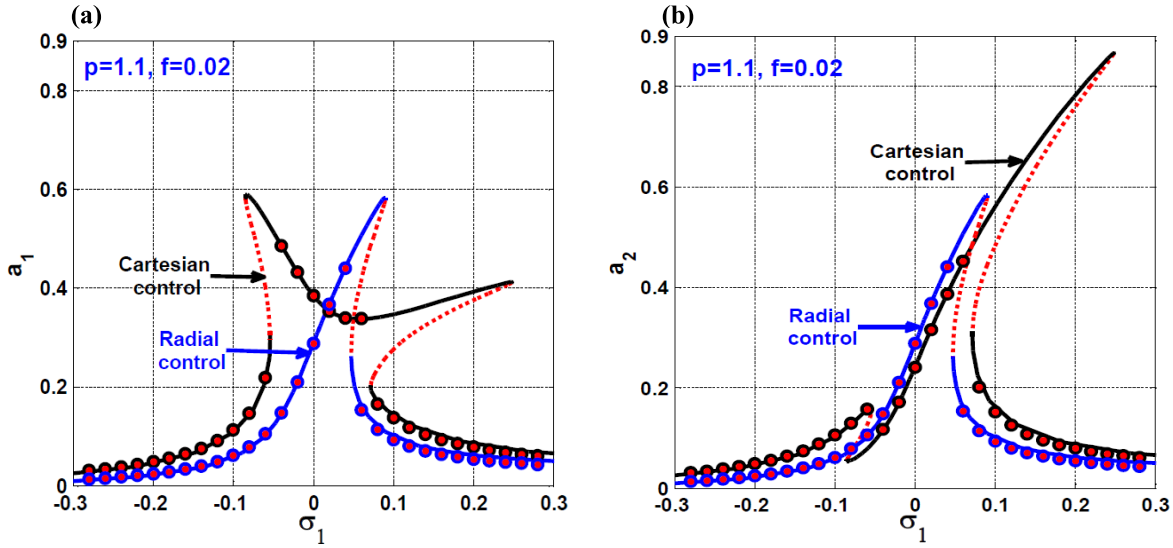

FIGURE 22. The 6-pole Rotor-AMBs spinning-speed response-curve at $f = 0.02$ and $p = 1.1$: (a) oscillation amplitude in $u-$direction, and (b) oscillation amplitude in $v-$direction.

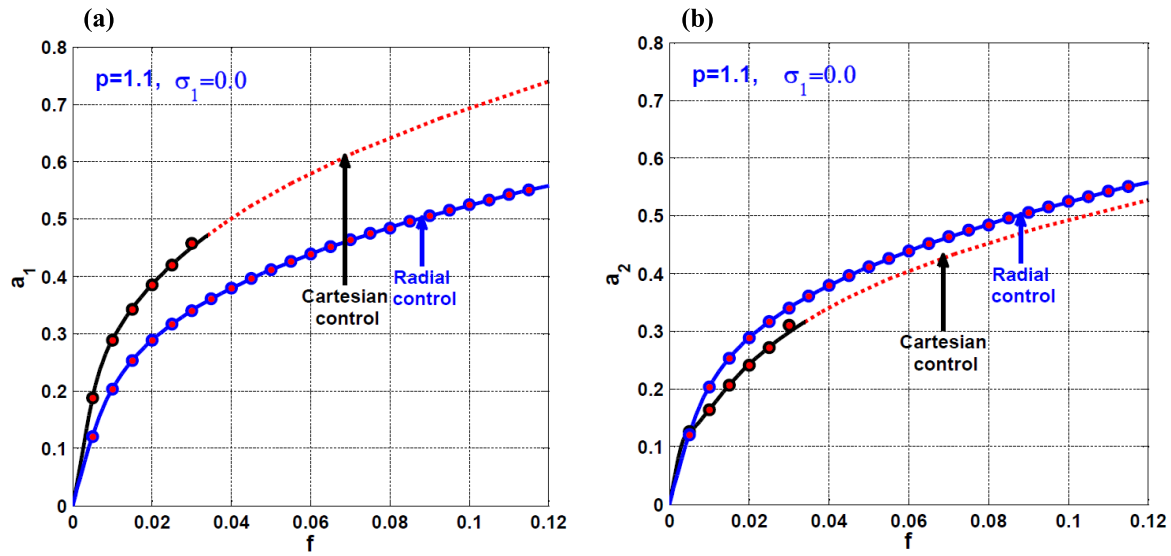

FIGURE 23. The 6-pole Rotor-AMBs eccentricity response-curve at $\sigma_1 = 0.0$ and $p = 1.1$: (a) oscillation amplitude in $u-$direction, (b) oscillation amplitude in $v-$direction.

strategies for the same system and control parameters. It is clear from Fig. 22 that the maximum oscillation amplitude in $u-$direction for the two control method are approximately the same, while at $v-$direction the radial control method is best. Moreover, under the cartesian control, the system can oscillate with high oscillation amplitude at a wide range of the disk spinning-speed and may be subjected to two consecutive jump phenomenon while crossing the critical speed. Besides, the system may oscillate with one of three whirling modes depending on the disk spinning-speed. On the other hand, when the radial control method is applied the system will perform symmetric oscillation amplitudes in u and $v-$directions that leading to circular forward whirling motion regardless of the disk spinning speed. Fig. 23 compares the system eccentricity response-curve under the applied control methods when $\sigma_1 = 0.0$, it is clear from the figure the symmetry of the system motion in the radial control method. Moreover, the system lateral vibrations are stable for the wide range of the disk eccentricity, while the system may lose its stability in the cartesian control method. Fig. 24 simulates numerically the system lateral vibrations according to Fig. 23 at $f = 0.06$ when the control method is online switched from the cartesian to the radial one at $t = 600$. The figure illustrates that the quasi-periodic motion of the system under cartesian control is stabilized when the radial controller is switched on after turning off the cartesian controller.

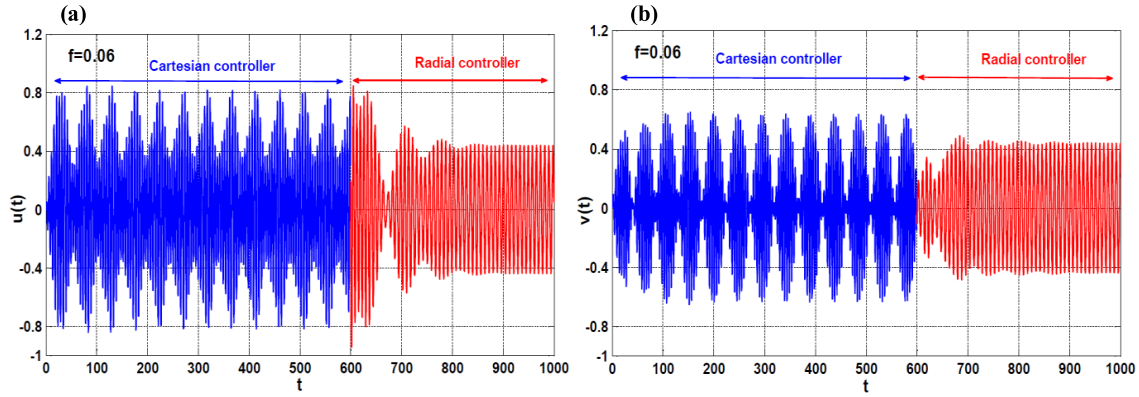

FIGURE 24. The system temporal oscillations according to Fig.23 when $f = 0.06$, where the control method is switched online from cartesian to radial one at $t = 600$: (a) oscillation amplitude in $u-$directions, and (b) oscillation amplitude in $v-$directions.

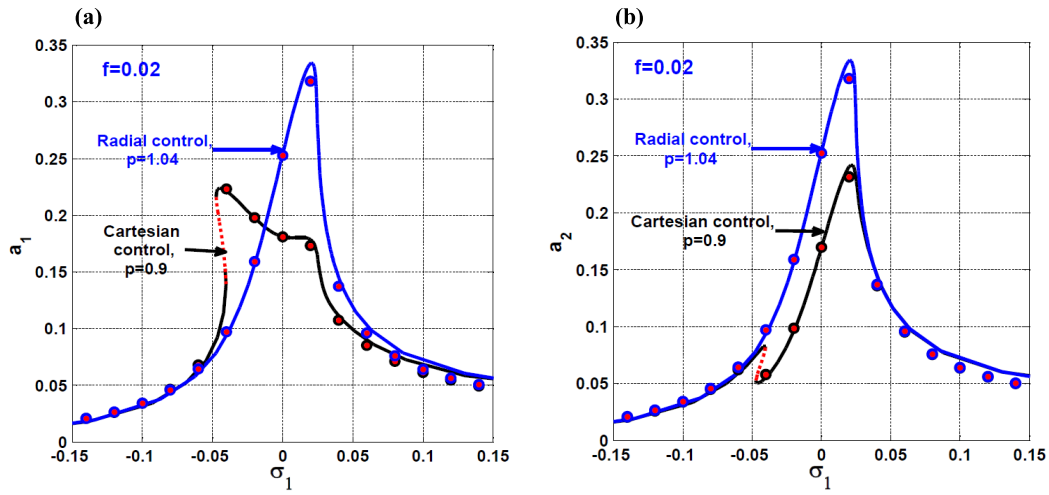

FIGURE 25. The 6-pole Rotor-AMBs spinning-speed response-curve at $f = 0.02$: (a) oscillation amplitude in $u-$direction, and (b) oscillation amplitude in $v-$direction.

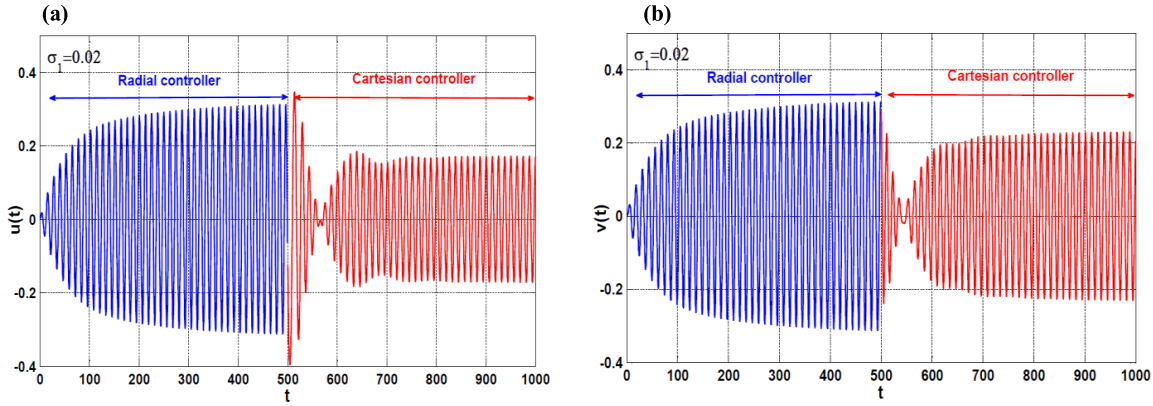

FIGURE 26. The system temporal oscillations according to Fig.24 when $\sigma_1 = 0.0$, where the control method is switched online from radial to cartesian one at $t = 500$: (a) oscillation amplitude in $u-$directions, and (b) oscillation amplitude in $v-$directions.

Based on the discussion given in section *IV-A* and *IV-B*, it is reported that the proportional control gain has a great influence on the system dynamics either in radial or cartesian control strategies. Accordingly, the system spinning-speed response curves under both the radial and cartesian control methods at the optimal value of the proportional control gain are compared in Fig. 25. It clear from the figure that both the radial and cartesian control strategies approximately have the same performance in suppressing the system lateral vibrations when $\sigma_1 \leq -0.05$ and $\sigma_1 \geq 0.05$, but for

TABLE 1. Comparison between the radial and cartesian control methods.

Items	Radial control method	Cartesian control method
Stability range of the proportional gain (p):	$1 < p \leq 1.18$	$\frac{\sqrt{3}}{2} < p \leq 1.1$
Optimum proportional gain (p):	$p = 1.04$	$p = 0.9$
Efficiency at the same value of the proportional gain (p):	High efficiency control method	Low efficiency control method
Efficiency at the optimum value of the proportional gain (p):	Low efficiency control method	High efficiency control method
The robustness against system instability (at large disk eccentricity):	Robust control method	Not robust control method (i.e. the system may exhibits quasiperiodic motions)
The system oscillation modes:	Circular forward whirling motions only are noticed	Forward whirling, backward whirling, both forward and backward whirling, and oscillation along a straight line are noticed

$-0.05 < \sigma_1 < 0.05$, the cartesian control method exhibits high performance than the radial one. Fig. 26 numerically simulates the system lateral vibrations according to Fig. 25 at $\sigma_1 = 0.0$ when the control strategy is online switched from the radial to the cartesian one at $t = 500$. It is clear that the oscillation amplitudes in u and $v-$directions are clearly mitigated when the cartesian controller is switched on after turning off the radial controller. Accordingly, a comparative study between the radial and cartesian control method is summarized as given in Table 1.

V. CONCLUSION

This paper is intended to discuss two different control techniques to mitigate the nonlinear lateral vibrations of the 6-pole Rotor-AMBs. The two applied control methods are designed based on the proportional-derivative current controller. In the first control method, the control current in each pole is designed to be proportional to both the radial displacement and the radial velocity of the rotating disk toward that pole. In the second method, the control current is proposed to be proportional to both the cartesian displacement and the cartesian velocity of the rotating disk in two perpendicular directions. The system mathematical model for each control method is derived and then analyzed by applying asymptotic analysis. The system dynamical behaviors under the applied control methods are compared utilizing response-curves, bifurcation diagrams, and numerical simulations. Based on the presented results the following important remarks can be concluded:

1. The 6-pole Rotor-AMBs under the radial control strategy exhibits symmetric oscillation amplitudes in u and $v-$direction, which ultimately leads to a circular forward whirling motion only.
2. The 6-pole Rotor-AMBs under cartesian control technique can oscillate with one of four whirling modes (that are forward, backward, both forward and backward, and along a straight line) depending on the disk spinning-speed and the system initial conditions.
3. The 6-pole Rotor-AMBs may be subjected to one jump phenomenon while the disk spinning-speed crossing the system critical speed in the radial control case, but two consecutive jump phenomenon are expected in the cartesian control strategy.
4. The proportional control gain (p) plays a very important role in stabilizing the considered system and improving the vibration suppression efficiency, where increasing p beyond specific limit increases the oscillation amplitudes and can destabilize the system motion either in the radial or in the cartesian control.
5. To guarantee the system stability, the proportional control gain should be kept within the range $1 < p \leq 1.18$ in the case of the radial control, while in the cartesian control method p should be $\frac{\sqrt{3}}{2} < p \leq 1.1$.
6. Although the cartesian control method has vibration suppression efficiency higher than the radial control one, the radial control method is more robust against the system instability especially if Rotor-AMBs has large disk eccentricity.
7. According to the concluded point 6, it is possible to implement the two control strategies on a digital controller that can be programmed to select the optimal control method depending on the required operational conditions.

ACKNOWLEDGMENT

The authors are grateful to the Researchers Supporting Project number (RSP-2020/164), King Saud University, Riyadh, Saudi Arabia.

REFERENCES

[1] J. C. Ji, L. Yu, and A. Y. T. Leung, "Bifurcation behavior of a rotor supported by active magnetic bearings," *J. Sound Vib.*, vol. 235, no. 1, pp. 133–151, Aug. 2000.

[2] J. C. Ji and C. H. Hansen, "Non-linear oscillations of a rotor in active magnetic bearings," *J. Sound Vib.*, vol. 240, no. 4, pp. 599–612, Mar. 2001.

[3] J. C. Ji and A. Y. T. Leung, "Non-linear oscillations of a rotor-magnetic bearing system under superharmonic resonance conditions," *Int. J. Non-Linear Mech.*, vol. 38, no. 6, pp. 829–835, Sep. 2003.

[4] N. A. Saeed, M. Eissa, and W. A. El-Ganini, "Nonlinear oscillations of rotor active magnetic bearings system," *Nonlinear Dyn.*, vol. 74, nos. 1–2, pp. 1–20, Oct. 2013.

[5] M. Eissa, N. A. Saeed, and W. A. El-Ganini, "Saturation-based active controller for vibration suppression of a four-degree-of-freedom rotor–AMB system," *Nonlinear Dyn.*, vol. 76, no. 1, pp. 743–764, 2014.

[6] N. A. Saeed and A. Kandil, "Lateral vibration control and stabilization of the quasiperiodic oscillations for rotor-active magnetic bearings system," *Nonlinear Dyn.*, vol. 98, no. 2, pp. 1191–1218, Oct. 2019.

[7] W. Zhang and X. P. Zhan, "Periodic and chaotic motions of a rotor-active magnetic bearing with quadratic and cubic terms and time-varying stiffness," *Nonlinear Dyn.*, vol. 41, no. 4, pp. 331–359, Sep. 2005.

[8] W. Zhang, M. H. Yao, and X. P. Zhan, "Multi-pulse chaotic motions of a rotor-active magnetic bearing system with time-varying stiffness," *Chaos, Solitons Fractals*, vol. 27, no. 1, pp. 175–186, Jan. 2006.

[9] W. Zhang, J. W. Zu, and F. X. Wang, "Global bifurcations and chaos for a rotor-active magnetic bearing system with time-varying stiffness," *Chaos, Solitons Fractals*, vol. 35, no. 3, pp. 586–608, Feb. 2008.

[10] R. Wu, W. Zhang, and M. H. Yao, "Nonlinear vibration of a rotor-active magnetic bearing system with 16-pole legs," in *Proc. Int. Design Eng. Tech. Conf. Comput. Inf. Eng. Conf.*, vol. 58202, Aug. 2017, Art. no. V006T10A037.

[11] R. Q. Wu, W. Zhang, and M. H. Yao, "Nonlinear dynamics near resonances of a rotor-active magnetic bearings system with 16-pole legs and time varying stiffness," *Mech. Syst. Signal Process.*, vol. 100, pp. 113–134, Feb. 2018.

[12] W. Zhang, R. Q. Wu, and B. Siriguleng, "Nonlinear vibrations of a rotor-active magnetic bearing system with 16-pole legs and two degrees of freedom," *Shock Vib.*, vol. 2020, pp. 1–29, Jan. 2020.

[13] A. Kandil, M. Sayed, and N. A. Saeed, "On the nonlinear dynamics of constant stiffness coefficients 16-pole rotor active magnetic bearings system," *Eur. J. Mech.-A/Solids*, vol. 84, Nov. 2020, Art. no. 104051, doi: 10.1016/j.euromechsol.2020.104051.

[14] J. Tang, J. Fang, and W. Wen, "Superconducting magnetic bearings and active magnetic bearings in attitude control and energy storage flywheel for spacecraft," *IEEE Trans. Appl. Supercond.*, vol. 22, no. 6, Dec. 2012, Art. no. 5702109.

[15] J. Tang, K. Wang, and B. Xiang, "Stable control of high-speed rotor suspended by superconducting magnetic bearings and active magnetic bearings," *IEEE Trans. Ind. Electron.*, vol. 64, no. 4, pp. 3319–3328, Apr. 2017.

[16] T. Du, H. Geng, Y. Zhang, H. Lin, Y. Li, and L. Yu, "Exact analytical method for active magnetic bearings with rotor eccentricity," *IEEE Trans. Magn.*, vol. 55, no. 12, pp. 1–12, Dec. 2019.

[17] S. Xu, X. Liu, and Y. Le, "Electromagnetic design of a high-speed solid cylindrical permanent-magnet motor equipped with active magnetic bearings," *IEEE Trans. Magn.*, vol. 53, no. 8, pp. 1–15, Aug. 2017.

[18] Y. Zheng, N. Mo, Y. Zhou, and Z. Shi, "A model-free control method for synchronous vibration of active magnetic bearing rotor system," *IEEE Access*, vol. 7, pp. 79254–79267, 2019.

[19] Y. Zheng, N. Mo, Y. Zhou, and Z. Shi, "Unbalance compensation and automatic balance of active magnetic bearing rotor system by using iterative learning control," *IEEE Access*, vol. 7, pp. 122613–122625, 2019.

[20] X. Yao, Z. Chen, and Y. Jiao, "A dual-loop control approach of active magnetic bearing system for rotor tracking control," *IEEE Access*, vol. 7, pp. 121760–121768, 2019.

[21] H. Gao, X. Meng, and K. Qian, "The impact analysis of beating vibration for active magnetic bearing," *IEEE Access*, vol. 7, pp. 134104–134112, 2019.

[22] Y. Ishida and T. Inoue, "Vibration suppression of nonlinear rotor systems using a dynamic damper," *J. Vib. Control*, vol. 13, no. 8, pp. 1127–1143, Aug. 2007.

[23] N. A.-F. Abdul-Hameed Saeed and M. Kamel, "Nonlinear PD-controller to suppress the nonlinear oscillations of horizontally supported jeffcott-rotor system," *Int. J. Non-Linear Mech.*, vol. 87, pp. 109–124, Dec. 2016.

[24] N. A. Saeed and M. Kamel, "Active magnetic bearing-based tuned controller to suppress lateral vibrations of a nonlinear jeffcott rotor system," *Nonlinear Dyn.*, vol. 90, no. 1, pp. 457–478, Oct. 2017.

[25] N. A. Saeed and H. A. El-Gohary, "Influences of time-delays on the performance of a controller based on the saturation phenomenon," *Eur. J. Mech.-A/Solids*, vol. 66, pp. 125–142, Nov. 2017.

[26] N. A. Saeed and W. A. El-Ganaini, "Utilizing time-delays to quench the nonlinear vibrations of a two-degree-of-freedom system," *Meccanica*, vol. 52, nos. 11–12, pp. 2969–2990, Sep. 2017.

[27] N. A. Saeed and W. A. El-Ganaini, "Time-delayed control to suppress the nonlinear vibrations of a horizontally suspended jeffcott-rotor system," *Appl. Math. Model.*, vol. 44, pp. 523–539, Apr. 2017.

[28] R. S. Srinivas, R. Tiwari, and C. Kannababu, "Application of active magnetic bearings in flexible rotordynamic systems–A state-of-the-art review," *Mech. Syst. Signal Process.*, vol. 106, pp. 537–572, Jun. 2018.

[29] K. Matsuda, Y. Kanemitsu, and S. Kijimoto, "Optimal number of stator poles for compact active radial magnetic bearings," *IEEE Trans. Magn.*, vol. 43, no. 8, pp. 3420–3427, Aug. 2007.

[30] G. Schweitzer and E. H. Maslen, *Magnetic Bearings: Theory, Design, and Application to Rotating Machinery*, vol. 1. Berlin, Germany: Springer, 2009.

[31] Y. Ishida and T. Yamamoto, *Linear and Nonlinear Rotordynamics: A Modern Treatment With Applications*. Hoboken, NJ, USA: Wiley, 2013.

[32] H. M. Sedighi, K. H. Shirazi, and J. Zare, "An analytic solution of transversal oscillation of quintic non-linear beam with homotopy analysis method," *Int. J. Non-Linear Mech.*, vol. 47, no. 7, pp. 777–784, Sep. 2012.

[33] H. M. Sedighi, K. H. Shirazi, and J. Zare, "Novel equivalent function for deadzone nonlinearity: Applied to analytical solution of beam vibration using He's parameter expanding method," *Latin Amer. J. Solids Struct.*, vol. 9, no. 4, pp. 443–452, Aug. 2012.

[34] M. A. Eltaher, N. Mohamed, S. A. Mohamed, and L. F. Seddek, "Periodic and nonperiodic modes of postbuckling and nonlinear vibration of beams attached to nonlinear foundations," *Appl. Math. Model.*, vol. 75, pp. 414–445, Nov. 2019.

[35] M. A. Eltaher and N. Mohamed, "Nonlinear stability and vibration of imperfect CNTs by doublet mechanics," *Appl. Math. Comput.*, vol. 382, Oct. 2020, Art. no. 125311.

[36] A. H. Nayfeh and D. T. Mook, *Nonlinear Oscillations*. New York, NY, USA: Wiley, 1979.

NASSER A. SAEED was born in Menoufia, Egypt, in 1986. He received the B.S. degree in industrial electronics and control engineering from the Department of Industrial Electronics and Control Systems, Faculty of Electronic Engineering, Menoufia University, Egypt, in 2008, and the M.S. and Ph.D. degrees in engineering mathematics from the Department of Physics and Engineering Mathematics, Faculty of Electronic Engineering, Menoufia University, in 2014 and 2018, respectively. Since 2018, he has been an Assistant Professor with the Department of Physics and Engineering Mathematics, Faculty of Electronic Engineering, Menoufia University. He is the author of more than 20 articles published in high reputable journals. He developed his researches in the field of nonlinear dynamics, bifurcation theory, linear and nonlinear vibrations control, perturbation methods, rotor-dynamics, and rotor active magnetic bearings systems.

EMAD MAHROUS AWWAD was born in Menia, Egypt, in 1988. He graduated in 2011. He is currently pursuing the Ph.D. degree with the Department of Electrical Engineering, King Saud University. He employed as a Teaching Assistant at the Department of Industrial Electronics and Control Engineering, Faculty of Electronic Engineering, Menofia University, Egypt, in 2012. He developed his researches in the field of system design, control of linear and nonlinear systems, embedded system design, the Internet of Things (IoT), and implementation of autonomous mobile robot. He is interested in modeling, optimization, and observer design and model predictive controller of vehicle dynamics under the wheel-terrain interaction slippage phenomenon. He is also interested in artificial intelligent, machine learning, and deep learning related to the field of robotics and image processing.

MOHAMMED A. EL-MELIGY received the B.Sc. degree in information technology from Menoufia University, Egypt, in 2005. He has been a Software Engineer with King Saud University, Riyadh, Saudi Arabia, since 2009. His research interests include Petri nets, supervisory control of discrete event systems, database software, and network administration.

EMAD S. ABOUEL NASR received the Ph.D. degree in industrial engineering from the University of Houston, Houston, TX, USA, in 2005. He is currently a Professor with the Department of Industrial Engineering, College of Engineering, King Saud University, Saudi Arabia, and an Associate Professor with the Department of Mechanical Engineering, Faculty of Engineering, Helwan University, Egypt. His current research interests include CAD, CAM, rapid prototyping, advanced manufacturing systems, and collaborative engineering.